SOUTHERN CALIFORNIA
EDISON
An *EDISON INTERNATIONAL*℠ Company

Dwight E. Nunn
Vice President

December 27, 2001

U.S. Nuclear Regulatory Commission
Attention: Document Control Desk
Washington, D.C. 20555-0001

Subject: Docket Nos. 50-361 and 50-362
Seismic Design Basis Assessment
San Onofre Nuclear Generating Station, Units 2 and 3

References:
1. August 2, 2001 letter from NRC (S. Dembeck) to SCE (H. B. Ray), Subject: San Onofre Nuclear Generating Station Seismic Design Basis
2. September 21, 2001 letter from D. E. Nunn (SCE) to the NRC (Document Control Desk), Subject: Seismic Design Basis Assessment, San Onofre Nuclear Generating Station, Units 2 and 3
3. December 15, 1995 letter from W. C. Marsh (SCE) to the NRC (Document Control Desk), Subject: Response to Generic Letter 88-20, Supplement 4, Individual Plant Examination of External Events (IPEEE), San Onofre Nuclear Generating Station, Units 2 and 3

Gentlemen:

This letter provides the final response to the information requested in the August 2, 2001 NRC letter (Reference 1) concerning the seismic design basis for San Onofre Units 2 and 3. As requested, Southern California Edison (SCE) has reviewed the statements by Dr. Mark Legg in item 2 of his comments in Reference 1.

As stated in Reference 2, SCE's initial response to Reference 1, there is a great deal of uncertainty as to the Oceanside detachment/thrust fault system's location, extent, and seismogenic potential, and no definitive conclusions could be drawn as to the significance of the postulated fault from the references cited by Dr. Legg. Therefore, SCE conducted a study to evaluate whether the postulated blind thrust fault would have any significant effect on the seismic risk of San Onofre Units 2 and 3 using the seismic risk methodology used for the Individual Plant Examination of External Events (IPEEE) (Reference 3) and supplementing it with the latest available information in the vicinity of San Onofre.

The report of the "Seismic Hazard Study of Postulated Blind Thrust Faults, San Onofre Nuclear Generating Station, Units 2 and 3" is enclosed. A seismic source characterization was developed, global positioning system data was reviewed to assess

P. O. Box 128
San Clemente, CA 92674-0128
949-368-1480
Fax 949-368-1490

A073

the reasonableness of the source characterization, a probabilistic seismic hazard analysis was performed using the most current published attenuation relationships, and the effect of the revised seismic hazard curve on the seismic risk at San Onofre was evaluated. The probabilistic risk analysis results show that there would be no seismic vulnerabilities at San Onofre and the increase in core damage frequency is small. Therefore, the postulated blind thrusts would not appreciably change the seismic risk of San Onofre Units 2 and 3.

If you have any questions or would like additional information, please contact me or Mr. Jack L. Rainsberry (949/368-7420).

Sincerely,

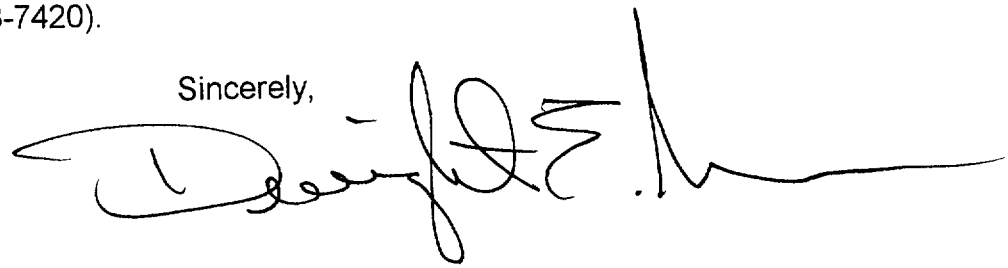

Enclosure

cc: E. W. Merschoff, Regional Administrator, NRC Region IV
J. N. Donohew, NRC Project Manager, San Onofre Units 2, and 3
C. C. Osterholtz, NRC Senior Resident Inspector, San Onofre Units 2 & 3

SAN ONOFRE NUCLEAR GENERATING STATION

UNITS 2 AND 3

SEISMIC HAZARD STUDY OF POSTULATED BLIND THRUST FAULTS

December 26, 2001

Prepared by:

Geomatrix Consultants

GeoPentech

Southern California Edison

TABLE OF CONTENTS

LIST OF TABLES

LIST OF FIGURES

LIST OF PLATES

EXECUTIVE SUMMARY

Southern California Edison (SCE) has conducted a study to determine whether recently postulated blind thrust faults in the vicinity of San Onofre would have a significant effect on the seismic risk of the San Onofre Nuclear Generating Station (SONGS), Units 2 and 3. The study is a follow-up to the initial assessment that was provided in an SCE letter to the NRC dated September 21, 2001 and is in response to an NRC letter to SCE dated August 2, 2001.

The study was performed using the seismic hazard data from the seismic risk analysis for the SONGS Individual Plant Examination of External Events (IPEEE) (SCE letter dated December 15, 1995) and supplementing it with the latest available seismicity information in the vicinity of SONGS.

The seismic source characterization was primarily developed by Geomatrix Consultants and involved several other consultants. GeoPentech was responsible for the probabilistic seismic hazard analysis using the three seismic source models developed by Geomatrix Consultants. In addition, GeoPentech conducted a review of global positioning system data to assess the reasonableness of the weights assigned to the seismic source models. SCE evaluated the effect of the revised seismic hazard curve on the seismic risk at SONGS.

Seismic Source Characterization

The seismic source characterization model developed for this study updates the source model previously developed as part of the seismic risk analysis for the SONGS IPEEE (SCE letter dated December 15, 1995; Risk Engineering, 1995, Appendix A). In particular this study evaluated recently postulated blind thrust faults in the vicinity of SONGS (i.e., the Oceanside blind thrust (OBT) and San Joaquin Hills blind fault (SJBF)) that were not explicitly modeled in the IPEEE study. For this study, three alternative source characterization models were developed to capture the range of plausible fault source geometries and interactions between the postulated thrust and strike-slip faults that could have a significant impact on the seismic hazard to SONGS.

Model 1 assumes that there is a through-going strike slip fault system (the Newport Inglewood – South Coast Offshore Zone of Deformation – Rose Canyon system (NI-SCOZD-RC)) that extends to seismogenic depth. In this model the Oceanside detachment is not considered to be an active seismogenic source. A blind thrust fault underlying the San Joaquin Hills (the SJBF) is included as a potential seismogenic fault source with a probability of activity (i.e., it behaves as an independent seismic source) of 0.5.

Model 2 assumes the Oceanside blind thrust (OBT) to be an active seismogenic source. Two alternatives are considered, depending on whether or not the San Joaquin Hills blind fault (SJBF) is linked (i.e., is a backthrust) to the OBT. The NI and RC are modeled as independent strike-slip faults.

Model 3- In this model, the OBT and SCOZD-RC represent strain partitioning in the upper crust (thrust and strike-slip, respectively) above a single oblique-slip fault plane (OBT-oblique) at depth. The NI is modeled as an independent strike-slip fault.

Based on consideration of the evidence for the activity and seismogenic potential of these faults, as well as geologic and geodetic evidence that pertain to the style and rate of deformation that is occurring in the present tectonic environment, weights were assigned to the models as follows: Model 1 (0.7); Model 2 (0.25); and Model 3 (0.05). Although there is general agreement in the professional and academic communities that detachment faults are present in the inner California borderland, there is no direct evidence that clearly demonstrates that these faults have been reactivated as blind thrust faults on a regional scale. Evidence presented by Rivero and others (2000) regarding the level of activity, slip rate, and seismogenic potential of the OBT as a source of future large magnitude earthquakes is inconclusive.

A much stronger case is made in support of the model that characterizes the South Coast Offshore Zone of Deformation (SCOZD) as part of a through-going strike-slip fault zone. The chief arguments supporting the higher weight given to the strike-slip model (Model 1) are:

- Interpretations of 2D and high-resolution shallow seismic data show evidence for a relatively continuous zone of recent deformation linking the RC and NI. Seismicity and paleoseismic data show that the NI and RC faults are capable strike-slip faults.

- Geodetic data show that strain in the southern Californian inner borderland is characterized by north-northwest directed shear subparallel to the overall North America/Pacific plate motion. Little or no convergence across the inner borderland in the vicinity of SONGS is indicated in the geodetic data. In particular, the lack of significant convergence in the regional signal to the east of the OBT suggests there is not a regional "driving" force that would reactivate a large seismogenic thrust.

- Fault and fold deformation observed along the SCOZD is consistent with transpressional right lateral slip along a N20°W trending fault. Evidence to support reactivation of the entire OBT in the current tectonic environment is not demonstrated. Seismicity and possible late Pleistocene/Holocene faults and associated folding can be explained by localized reactivation (strain partitioning) and contraction in left steps or bends in a transpressional right-slip tectonic environment. Clockwise rotation of crustal blocks in the inner borderland, which is not inconsistent with geodetic data that suggests a component of extension cross the southern inner borderland, could account for the greater intensity of contractional structures in the hanging wall of the northern OBT west of the SCOZD. This might explain the local reactivation of portions of the OBT, but would not require reactivation or rupture of the entire detachment.

- Much of the contractional deformation observed in the inner borderland (e.g., the San Mateo thrust belt and the Carlsbad thrust) could have occurred during the Pliocene within a different stress regime.

- Regional coastal uplift, which is cited by Rivero and others (2000) to propose that the Oceanside and Thirtymile Bank thrusts are active over a region larger than the San Joaquin Hills, may be attributed to a large degree to other processes (e.g., rift shoulder thermal isostasy). There is no evidence for tilting or significant differential uplift along the coast as recorded by the Quaternary marine terraces and underlying Tertiary bedrock that would indicate movement on an underlying thrust fault.

Global Positioning System Data Evaluation

Recorded tectonic ground displacement rates from the Global Positioning System (GPS) stations in southern California were systematically used to assess implications of the postulated Oceanside blind thrust (OBT). Evaluation of GPS data provides a check on the overall reasonableness of the postulated OBT and weights assigned to different seismic source characterization models (Model 1, Model 2, and Model 3).

On the basis of a systematic evaluation of GPS data performed in this study, the following observations can be made:

- The overall patterns of relative displacement rates indicate that no compressional relative displacement fields exist behind the hanging wall side of the OBT postulated as part of Model 2 and Model 3.

- Both the total and incremental relative displacement rates associated with the four selected pairs of SCIGN GPS stations are adequately consistent with the slip rates associated with Model 1 fault sources.

- Both the total and incremental relative displacement rates associated with the four selected pairs of SCIGN GPS stations appear to become significantly inconsistent with the slip rates associated with the postulated Model 2 and Model 3 fault sources, with Model 3 being slightly less consistent than Model 2. Although for some pairs the consistency may improve for Model 2 and Model 3, it is the overall pattern of consistency that dictates the reasonableness of the postulated seismic sources.

- There may be some compressive strain occurring between some coastal areas near the SONGS site and Catalina Island. However, the reported error ellipses associated with these sites are large enough that the compressive component may well be within the uncertainties, and, in any case, the small compressive strain that may be occurring between the coastal area and Catalina Island is considered inadequate to load or drive the postulated OBT.

- A systematic evaluation of the available GPS data indicates that assigning weights to Model 2 and Model 3 higher than those presented in Section 2.0 is not justified. On the contrary, based strictly on the GPS data, one can make a good case for assigning weights significantly lower than those presented in Section 2.0 for Model 2 and Model 3.

- Finally, it is noted that where the patterns of GPS relative displacement rates indicate significant unaccounted compressional components in a region in the direction perpendicular to the major strike-slip faults, a conclusion is often reached that thrust faults would likely accommodate the contraction (e.g., Bawden et al., 2001). The absence of such patterns of significant GPS relative displacement rates in the direction perpendicular to the major strike-slip faults in the inner California borderland makes it difficult to postulate significant active thrust faults in the vicinity of SONGS.

Seismic Hazard Analysis

Probabilistic seismic hazard analysis (PSHA) was performed to evaluate the spectral acceleration values for the SONGS site using the seismic sources in this study. The probabilistic results of the SONGS IPEEE work are used as the baseline, and the 2001 PSHA results for Model 1 are used as the basis to discuss the effects of OBT as reflected in Models 2 and 3 as well as the effects of near-fault directivity and fling step as a sensitivity study.

Compared to the SONGS IPEEE response spectrum, the 2001 PSHA response spectrum has slightly higher accelerations in the low frequencies range, but the results appear to be comparable as shown on Figure 4-21.

Figure 4-22 shows the 2001 weighted hazard curve for the combined results (Model 1, Model 2, and Model 3) reflecting the directivity and fling step effects. Figure 4-22 also shows the SONGS IPEEE weighted hazard curve for comparison. Overall the 2001 weighted hazard curve is comparable to the SONGS IPEEE weighted hazard curve.

Seismic Probabilistic Risk Analysis

In order to evaluate the effect of considering the postulated blind thrust faults on the seismic risk at SONGS, the seismic probabilistic risk analysis (PRA) was focused on the potential increase in core damage and large early release risk due to postulated blind thrusts. The SONGS Living PRA, which includes external events, was used to assess this potential increase. Since the submittal of the IPEEE (SCE letter to NRC dated December 15, 1995), the plant and the plant model have undergone a number of risk reducing plant modifications and model improvements, respectively. These improvements have been included in the SONGS Living PRA and are included in this study. The SONGS Living PRA reflects the as-built plant.

To calculate the risk impact of the postulated blind thrusts, the baseline risk is assessed using the current SONGS Living PRA. This is compared against the postulated risk as assessed by substituting the postulated seismic hazard curve in the current SONGS Living PRA. The risk difference, or risk increase, is evaluated for core damage frequency (CDF) and large, early release frequency (LERF).

The SONGS Living PRA model consists of the seismic hazard curve, seismic event tree, component fragilities, and the internal events PRA model. Except for the seismic hazard curve, all other model components remained constant in the calculation. The baseline seismic hazard curve for this calculation was developed for the SONGS IPEEE.

While the Uniform Hazard Spectrum exhibits some increases in spectral accelerations at low frequencies of less than 1.5 Hz, there would be negligible effects on the structural responses of the SONGS IPEEE buildings because the structures have natural frequencies of about 1.5 Hz and higher. The decrease in spectral accelerations at the higher frequencies above 1.5 Hz would have the effect of reducing the seismic demands on components. Therefore, the SONGS IPEEE seismic fragilities were not revised for input into the PRA model.

From the SONGS 2/3 Living PRA, the current average SONGS CDF and LERF from internal and external events are 4.27E-5/year and 1.60E-6/year, respectively. Substituting the seismic hazard curve to include the postulated blind thrusts results in a total average core damage and large, early release risk of 4.57E-5/year and 1.78E-6/year. These are postulated increases of 3.0E-6/year and 1.8E-7/year.

The PRA results show that there would be no seismic vulnerabilities at SONGS and the increase in core damage frequency is small. Therefore, the postulated blind thrusts would not appreciably change the seismic risk of SONGS.

1.0 INTRODUCTION

Southern California Edison (SCE) has conducted a study to evaluate whether recently postulated blind thrust faults in the vicinity of San Onofre would have a significant effect on the seismic risk of the San Onofre Nuclear Generating Station (SONGS) Units 2 and 3. The study is a follow-up to the initial assessment that was provided in an SCE letter to the NRC dated September 21, 2001 and is in response to an NRC letter to SCE dated August 2, 2001.

The study was performed using the seismic hazard data from the seismic risk analysis for the SONGS Individual Plant Examination of External Events (IPEEE) (SCE letter dated December 15, 1995) and supplementing it with the latest available seismicity information in the vicinity of SONGS.

Section 2.0 of this report describes the seismic source characterization and the current research on the postulated blind thrusts near SONGS. Section 3.0 provides information concerning Global Positioning System (GPS) data to substantiate the weighting used for the seismic hazard analysis. Section 4.0 describes the probabilistic seismic hazard analysis that was performed for this study and includes considerations for near-fault effects. Section 5.0 provides the effect on the seismic risk of the plant when considering the resulting uniform hazard spectra and the seismic hazard curve. Section 6.0 summarizes the conclusions of the study and Section 7.0 is a listing of the references.

Acknowledgement is given to the following individuals for their contribution to this study:

Seismic Source Characterization

Geomatrix Consultants – Kathryn Hanson, Michael Angell
Consultant – William Foxall
Fugro West – Jan Rietman
GeoPentech – John Waggoner

Seismic Hazard Analysis

GeoPentech – Yoshi Moriwaki, Phalkun Tan, John Barneich
Consultant - Norm Abrahamson
Kenneth Hudnut (Section 3.0)
Geomatrix Consultants – Robert Youngs

Reviewer

Consultant – Clarence Allen

2.0 SEISMIC SOURCE CHARACTERIZATION

The San Onofre Nuclear Generating Station (SONGS) lies within a broad deforming region at the boundary between the Pacific and North America plates. According to the NUVEL-1 plate motion model (DeMets and others, 1990), the rate of relative Pacific-North America motion in southern California is approximately 46 ± 1 mm/yr and oriented about N41°W. Relative motion between the plates is characterized by transpressive dextral shear and is accommodated largely by dextral strike slip centered along the San Andreas fault system and faults in the borderlands of southern and Baja California, and to a lesser degree, by a component of Basin and Range extension parallel to the plate boundary, extension in the Gulf of California, and contractional structures in the Transverse Ranges and Los Angeles basin region (Zoback and others, 1981; Weldon and Humphreys, 1986; Argus and Gordon, 1988; Stein and Yeats, 1989).

Four major subparallel, northwest-trending, right-lateral strike-slip fault zones that occur in the offshore region of southern California and northern Baja California, Mexico were characterized as significant seismic sources in the seismic hazard model developed for the IPEEE for SONGS (Risk Engineering, 1995). Westward from the coast, these zones are the Newport-Inglewood/South Coast Offshore Zone of Deformation (SCOZD)/Rose Canyon, Palos Verdes-Coronado Bank-Agua Blanca, San Diego Trough, and San Clemente-San Isidro fault zones (Figure 2-1).

Reactivation of Miocene detachment fault systems in the inner California borderland as blind thrusts in the current transpressional tectonic regime has been postulated by several researchers, including Legg and others (1992), Crouch and Suppe (1993), Nicholson and others (1996), Mueller and others (1998a and b), Grant and others (1999), and most recently Rivero and others (2000). The earlier studies suggested that the detachment fault systems had been reactivated locally (e.g., Crouch and Suppe, 1993) and such localized deformation was considered in the IPEEE study . More recent studies (e.g., Rivero and others, 2000) conclude that entire detachment systems have been reactivated suggesting more significant seismic sources may be present in the inner borderland region offshore southern California.

Whereas there is general agreement in the professional and academic communities that detachment faults are present in the inner California borderland, there remains a great deal of uncertainty regarding whether or not these faults have been reactivated as blind thrusts, the degree to which they have been reactivated along their entire length, and their behavior in the contemporary tectonic environment. Alternative structural models for the interaction of the postulated blind thrust faults and recognized active strike-slip faults (e.g., the Newport-Inglewood and Rose Canyon faults) have been postulated by Grant and others (1999), Mueller and others (1998a and b), and Rivero and others (2000).

Using the seismic hazard methodology outlined in Risk Engineering (1995) for the IPEEE, alternative seismic source characterization models that consider the postulated blind thrust faults have been developed for this study. These models were developed based on:

- review of geologic, geophysical, and seismological data in licensing documents previously developed for SONGS (e.g., Western Geophysical, 1972; SONGS 2&3 Updated Final Safety Analysis Report (FSAR), Moore, 1980, West, 1979).

- Review of recent published literature

- Limited inspection and interpretation of offshore Common Depth Point (CDP) and high resolution seismic data

- Discussions and communications with several researchers (C. Rivero, Dr. J. Shaw, Dr. T. Rockwell, Dr. M. Legg. Dr. K. Mueller, Dr. L. Grant, Dr. K. Hudnut, and Dr. Y. Bock). At the recent Annual Southern California Earthquake Center (SCEC) meeting (September 24-25, 2001) Carlos Rivero and Dr. John Shaw met with various members of the SCE project team (Kathryn Hanson, Michael Angell, Jan Rietman, Dr. William Foxall, and John Waggoner) and discussed at length their current thoughts and interpretations regarding the Inner California Borderlands thrust system. Subsequent to the meeting they provided additional data and information regarding the geometry and rate of slip for the Oceanside blind thrust.

The following sections describe the data and interpretations included in the alternative seismic source characterization models used to conduct sensitivity analyses of the potential impact of the postulated blind thrusts to seismic hazard at SONGS. A summary of the evidence for the Miocene extensional systems and the activity, location, and slip rate of the postulated reactivated faults as blind thrusts is discussed in Section 2.1. This is followed by a discussion in Section 2.2 of data and observations from other studies, including data sets developed as part of the licensing documents for SONGS Units 2 and 3, that support the active strike slip Newport-Inglewood-South Coast Offshore Zone of Deformation-Rose Canyon fault system (NI-SCOZD-RC) offshore from SONGS. The alternative structural interaction models and uncertainties in source characterization parameters are described in Sections 2.3 and 2.4.

2.1 POSTULATED BLIND THRUST FAULTS

The identification and characterization of active, seismogenic blind fault seismic sources is an ongoing research topic in southern California. In this section the current interpretations are presented regarding the activity, location, and slip rate of two recently postulated fault sources that are judged by several researchers to be potential significant seismic sources for SONGS: 1) the San Joaquin Hills blind fault; and 2) the Oceanside blind thrust.

2.1.1 San Joaquin Hills Blind Fault

Structural and geomorphic modeling of the geometry and location of marine terraces and stream drainage networks suggests that the San Joaquin Hills anticline in the southern Los Angeles basin is an actively growing anticlinal fold (Grant and others, 1997; Mueller, 1997; Mueller and others, 1998a). Maps and cross sections of folded marine terraces correlated to marine oxygen isotope stages 5a-13 (~80 to 480 ka) (Barrie and others, 1992; Mueller and others, 1998a), and maps of drainage networks indicate northwest propagation of the anticline consistent with a fault-bend fold developed above a NE-vergent blind thrust ramp (Grant and others, 1997; Mueller and others, 1998a). However, as noted by Grant and others (1999), the available data and geomorphic analysis do not provide detailed constraints on the geometry of the San Joaquin Hills blind thrust.

Rates of uplift of the San Joaquin Hills derived from U-series dating of corals from deposits that overlie the terrace platforms yield determinations of 0.21 to 0.27 mm/yr in the last 122 ka (Mueller and others, 1998a and 1998b; Grant and others, 1999). Well data in the water gap between Huntington Mesa and Newport Mesa to the northwest of the San Joaquin Hills indicate that the Holocene Talbert Aquifer also is deformed in a style consistent with the structural models developed from the marine terrace data (Grant and others, 1999). Evidence of uplift of antecedent drainages and Holocene marshes in the Newport Back Bay also suggest that this structure is active (Mueller and others, 1997 and 1998a; Grant and others, 1999, in press).

Mueller and others (1998a and 1998b) and Rivero and others (2000) correlate the San Joaquin Hills fold and underlying east-vergent thrust with a similar fold that is imaged on seismic reflection profiles from the adjacent offshore region (Figures 2-2 and 2-3). They interpret the east-vergent blind thrust to transfer slip from the underlying east-dipping Oceanside detachment (described in the following section) as part of a wedge thrust structure. A preliminary interpretation of one of the offshore lines is presented in Mueller and others (1998b) (Figure 2-3c). Based on analogy to this fold they infer a 19-25°west-dipping thrust fault that intersects the tip of an underlying northwest-vergent detachment at a depth of approximately 5 km. Based on the width of the east-dipping forelimb (~900m), which they correlated to the amount of fault slip on an east-vergent blind thrust having a dip of 19-25°, they estimate a fault slip rate of 0.50 to 0.84 mm/yr (Mueller and others, 1998b). Mueller and others (1998a) report a slip rate of 0.51 mm/yr based on an inferred dip of 30°. Grant and others (1999) estimate a slip rate for the San Joaquin Hills blind thrust of 0.42-0.79 mm/yr based on an inferred fault dip (20-30°) and measured uplift rate of 0.21-0.27 m/kyr.

Mueller and others (1998b) and Rivero and others (2000) do not consider the east–vergent blind thrust responsible for uplift of the San Joaquin Hills as a significant source of future earthquakes, based on its relatively shallow intersection (e.g., 5 km) with the underlying detachment as inferred from the correlation of the onshore fold to the offshore fold. Grant and others (1999), however, allow for an alternative structural interpretation. They state a preference "... to interpret movement of the San Joaquin Hills blind thrust to

be the product of partitioned strike slip and compressive shortening across the southern Newport-Inglewood fault zone..." (Grant and others, 1999, p. 1034). In response to assertions by Bender (2000) that the structure of the Newport-Inglewood fault makes a blind thrust model unattractive, Grant and others (2000) suggest that a strain partitioning model in which seismogenic blind thrusts created by transpressive strain partitioning co-exist with an adjacent active strike-slip fault (Lettis and Hanson, 1991; Stein and Ekstrom, 1992) is a viable model. Grant and others (2000) conclude that the San Joaquin Hills are rising in response to a potentially seismogenic, underlying blind fault that should be included in regional seismic hazard models.

2.1.2 Oceanside Blind Thrust

Several recent studies that have addressed the Neogene kinematic evolution of California's borderland region and the adjacent Transverse Ranges have identified low-angle normal faults (detachments) that formed by large-magnitude crustal extension beginning in latest Oligocene-earliest Miocene time (Legg and others, 1992; Crouch and Suppe, 1993; Nicholson and others, 1993, 1994, 1996; Bohannon and Geist, 1998). Generalized schematic sections illustrating the style of crustal extension that is inferred to have developed in the Los Angeles basin-inner continental borderland (LAB-IB) rift are shown in Figures 2-4 and 2-5. Offshore seismic data are interpreted to image a major, east-dipping low-angle normal fault that is responsible for tectonic "footwall uplift" (exhumation) in Miocene time of high-grade metamorphic rocks now exposed on Catalina Island (Crouch and Suppe, 1993; Bohannon and Geist, 1998). Bohannon and Geist (1998) refers to this fault as the Oceanside detachment fault (Figure 2-6). Recent mapping by Rivero and others (2000) extend the Oceanside detachment and another similar fault (the Thirtymile Bank detachment) south from Laguna Beach and Catalina Island, respectively, to the United States—Mexico international border (Figure 2-7).

The Oceanside detachment fault is defined in the seismic data by several aligned, high-amplitude reflections with gentle apparent dips from between 1 and 2 seconds TWTT (two way travel time) in the west to between 2 and 3 sec TWTT in the east (Figures 2-8A and 2-9). Based on a velocity model they developed, Rivero and Shaw conclude that the thrust surface dips at (13-15°) to the north of latitude 33°N and dips 23-25° to the south of this geographic reference (C. Rivero, written communication, September 28, 2001).

The eastward extent and dip of the detachment beneath the coastline in the vicinity of SONGS is not known. The Oceanside detachment is not visible as a coherent reflector in seismic data east of the outer shelf edge. Fischer and Mills (1991), Crouch and Suppe (1993) and Bohannon and Geist (1998) interpret a very steeply dipping to vertical Newport-Inglewood Zone of Deformation, South Coast Offshore Zone of Deformation and Rose Canyon fault zone (NI-RC) (referred to as the Newport Inglewood-South Coast Offshore Zone of Deformation-Rose Canyon (NI-SCOZD-RC) fault zone in Risk Engineering, 1995) in the vicinity of the outer shelf edge (Figures 2-9 and 2-10). The intersection of the Oceanside detachment and the interpreted high-angle strike slip fault is not clearly imaged in the seismic data. Fisher and Mills (1991) show the detachment to be

disrupted by the high angle faults. In contrast, Rivero and Shaw (personal communication, September 24, 2001) map a basement overhang in this region and suggest that where the detachment juxtaposes basement against basement it is not expressed as a distinct reflector (e.g., Figure 2-8A). The eastern limit of the Oceanside detachment surface as interpreted from seismic reflection data by Rivero is shown on Figure 2-11. Based on the absence of geologic evidence to suggest a steepening of the Oceanside detachment at or near the coastline, Rivero (personal communication, September 24, 2001) concludes that the detachment maintains a similar dip to the east beneath the coastline.

Tectonic inversion and reactivation of the detachment faults as thrusts has been noted locally. Between San Mateo Point and Oceanside, a 30-km-long fold and thrust belt underlies the continental slope seaward of the NI-SCOZD (Crouch and Bachman, 1989; Fischer and Mills, 1991) (Figures 2-10 and 2-12). Within this deformed belt, fold axes and thrust faults are between 2.5 and 8 km west of, and parallel to, the main trace of the NI-SCOZD. Crouch and Bachman (1989) and Crouch and Suppe (1993) interpret thrust faults within this belt as rooted into an older regional detachment that has become reactivated locally. They consider development of this fold and thrust belt to be the result of northeast-southwest shortening that is normal to, and decoupled from, the northwest-trending strike-slip deformation along the NI-SCOZD. They note that crustal shortening, which began during Pliocene time, appears to still be active based on the presence of folds that extend to the sea floor.

Fischer and Mills (1991) separate structures in this zone into an inner thrust-fault-fold complex, which they interpret as a part of the flower structure of the NI-SCOZD, and an outer thrust-fold complex (Figure 2-10). They note that the outer thrust complex appears to be cut by the main thrust fault of the inner complex. They infer that the thrust faults along the inner margin are active, as is evidenced by their surficial topographic expression and the displacement of Quaternary reflectors.

Rivero and others (2000) speculate that large portions of these detachments have been reactivated to form the Oceanside and Thirtymile Bank thrusts, which comprise the Inner California Borderlands blind thrust system. Based on growth strata in contractional folds above both the Oceanside and Thirtymile Bank thrusts, they also conclude that thrusting began in the Pliocene. They note that seafloor scarps associated with the shallow, east-vergent fold-and-thrust belt above the Oceanside thrust between Dana Point and Oceanside may reflect recent activity of the underlying thrust [Note that this fold coincides with the NI-RC fault as shown by Crouch and Suppe, (1993) and Fischer and Mills, 1991) and the complex anticline or anticlinoriam associated with the SCOZD as mapped in SONGS 2&3 FSAR and by Moore (1980)]. However, they acknowledge that this is not definitive due to the lack of precise age control on the seafloor sediments. They cite, as further evidence for activity, the correlation of the offshore fold to the onshore San Joaquin Hills fold that shows clear evidence of late Pleistocene uplift and fold deformation. As noted in the previous section, they interpret the postulated San Joaquin Hills blind thrust and the east-vergent fault-bend fold formed beneath the modern shelf-

slope break as a backthrust that soles into the Oceanside thrust, forming a structural wedge (Medwedeff, 1992; Mueller and others, 1998a and b).

Based on the geometry of the wedge thrust and coastal uplift inferred from studies of the marine terraces in the San Joaquin Hills, Rivero and others (2000) calculate a late Pleistocene slip rate for the Oceanside thrust of ~0.27-0.41 mm/yr. This slip rate yields an uplift rate above the Oceanside thrust in the absence of the backthrust, of 0.07-0.17 mm/yr. They note that this rate is compatible with the observed 0.13-0.17 mm/yr uplift rate of marine terraces south of the San Joaquin Hills, which extend to San Diego and into northern Mexico (Lajoie and others, 1979, 1992; Barrie and others, 1992; Kern and Rockwell, 1992) (Figure 2-13).

In addition to the seafloor fold scarps and local uplift of marine terraces by backthrusts associated with the Oceanside blind thrust, Rivero and others (2000) cite additional seismologic, geologic, and geodetic data to suggest recent activity on the Inner California Borderlands blind thrust system. The 1986 Oceanside earthquake (ML 5.3) and aftershocks as relocated by Astiz and Shearer (2000) define a 25-30° east-dipping surface that is consistent with the downdip projection of the Thirtymile Bank thrust (Figure 2-7B). Rivero and others (2000) suggest that this earthquake ruptured a small part of the thrust. They cite geodetic observations that indicate as much as 2 mm/yr of northeast-southwest (N43°E) convergence between Catalina Island and the coast (Kier and Mueller, 1999) and use this value to constrain a maximum slip rate for the Oceanside blind thrust of 2.2 mm/yr. As noted in Section 3.0, however, analysis of a longer and more recent geodetic data set shows evidence for little or no convergence between Santa Catalina Island and the coast.

Additional slip rate estimates have been completed recently by Rivero using structural techniques to construct deformed and restored scenarios to describe the evolution of the Oceanside thrust. Assuming an average velocity for the slip, and setting the beginning of the transpressional regime in the Late Pliocene (circa 3.6 Ma), Rivero obtains a conservative slip rate of 1.0 – 0.8 mm/yr for this fault within the plane of the structural section (written communication, October 16, 2001). He notes that uncertainties in this slip rate estimate stem from uncertainties in the timing of the inception of transpression in the region.

2.2 ALTERNATIVE GEOLOGIC INTERPRETATIONS

Previous studies completed in the inner borderland of southern California have concluded that most or all of the recent deformation relates predominantly to strike-slip faults that are the major seismogenic fault sources in the region (see discussion in Risk Engineering, 1995, Appendix A). A summary of the data and interpretations of the behavior and capability of the Newport-Inglewood (NI) zone of deformation, South Coast Offshore Zone of Deformation (SCOZD), and Rose Canyon (RC) fault zone as presented in the licensing documents for SONGS Units 2 and 3 and other publications is discussed in the following section. This is followed by a discussion of the relationship between the offshore folds and the active San Joaquin Hills fold. Judgements regarding the activity

and seismogenic capability of the postulated Oceanside blind thrust rely to a great degree on the postulated link between the onshore and offshore folds.

2.2.1 Strike-slip fault zone (Offshore Zone of Deformation)

The South Coast Offshore Zone of Deformation (SCOZD), as defined in the licensing documents for SONGS Units 2 and 3 (SONGS 2&3 Final Safety Analysis Report (FSAR)), aligns with the offshore Newport-Inglewood Zone of Deformation (NIZD) and the Rose Canyon fault zone (RCFZ) and on this basis was considered to be part of a continuous system of faulting referred to as the Offshore Zone of Deformation (OZD). [Note: The NIZD and RCFZ are hereafter referred to as Newport-Inglewood fault (NI) and Rose Canyon fault zone (RC).] However, as discussed in SONGS 2&3 FSAR, geologic and geophysical evidence suggests that the NI, SCOZD, and RC are separate and distinct structural entities that exhibit differing degrees of activity and thus differing earthquake potential (see Sections 2.5.1.1.3.4 and 2.5.1.1.3.12 of the SONGS 2&3 FSAR).

Geophysical investigations conducted by Western Geophysical (1972) provide the basis for characterizing the location, continuity, and style of deformation associated with the SCOZD. Maps showing interpreted faults that cut acoustic basement (Horizon C) and a younger Upper Miocene horizon (Horizon B) are provided on Plates 2-1 and 2-2.

As described in the SONGS 2&3 FSAR, the NI consists of a series of short, discontinuous, northwest-trending en-echelon, right-lateral faults, relatively shallow drag fold anticlines, and subsidiary normal and reverse faults. The zone is terminated to the northwest by the Malibu-Santa Monica fault zone. The apparent termination of the NI to the southeast is inferred to be offshore between Newport Beach and Laguna Beach at the San Joaquin Structural High some 40 kilometers northwest of San Onofre (Plate 2-1). Distributive faulting and the lack of folding in the Newport oil fields are noted as indicative of termination of this zone within the Los Angeles basin. The 1933 M_W 6.4 Long Beach earthquake that occurred in Huntington Beach is located along the NI (Figure 2-2). Waveform analysis of teleseismic bodywave records of this earthquake (Woodward-Clyde Consultants, 1979; Hauksson and Gross, 1991) indicate displacement was right slip on a N40-45° west-trending fault with near vertical dip of 80° northeast. Hauksson and Gross (1991) report a focal depth of 8-12 km; Woodward-Clyde Consultants (1979) report a depth of 10-13 km.

The SCOZD was identified as a continuous trace within a zone of en-echelon faults in the acoustic basement (Western Geophysical, 1972). The fault zone extends approximately 67 km from its northern terminus approximately 8 km south of Newport Beach to its southern terminus southwest of Oceanside. At the northern terminus of the zone, displacements die out on the acoustic basement (believed to be Catalina Schist) near a north-south fault along the west side of the San Joaquin structural high. The closest approach of the SCOZD to SONGS is approximately 8 km to the southwest. Local northwest- to west-trending folds in the shallower horizons are also associated with this zone, and together with the faults, appear to reflect a tectonic style similar to that of the

NI. The interpretations of the geophysical data show the individual faults to be most continuous within the acoustic basement, Horizon C, and less continuous in the younger rocks, such as those represented by Horizon B (Plates 2-1 and 2-2, respectively). The apparent vertical fault displacements diminish rapidly in both the northwest and southeast directions from the central part of the zone. Similarly, displacements diminish upward in the section. Variations among the structural patterns through time are interpreted to be the result of two different tectonic regimes: (1) structures along the SCOZD on Horizon C appear to be dominated by north- and northwest-oriented normal faulting suggesting a period of east-west tension across the area; and (2) structures in Horizon B are consistent with a north-south compressional environment.

Detailed interpretations of the faulting within the SCOZD offshore SONGS are presented in Plate 2-3 as a geological cross section and an annotated copy of a seismic reflection line. The geological cross section begins approximately 12.2 km (7.5 miles) offshore and trends northeast through the SONGS site and across the Cristianitos fault. It is a compilation from several sources (including offshore seismic line WS-70-18) and modified (for text clarity and extended to the southwest) from a similar section presented by West (1979). The annotated seismic section, line W-10, is parallel to, and 4.1 km (2.6 miles) northwest of the geological cross section. The northeast extension of seismic line W-10 would intersect the coastline at San Mateo Point. The annotations on the seismic section represent the "B" and "C" horizons and near vertical fault strands as mapped by Western Geophysical (1972). In addition, a northeast dipping reflector that is interpreted to represent the Oceanside detachment fault is highlighted to illustrate the potential relationship with the near vertical strands of the SCOZD.

The ocean bottom in the illustrated sections ranges from sea level to approximately 760 meters (2500 feet). The seafloor slope is very gentle from the shoreline out to the eastern strand of the SCOZD. Steeper slopes are noted across the SCOZD and on the western slope of a fold at shot points (SP) 115 to 120 on line W-10 and SP 210 to 220 on line WS-70-18. These changes in ocean bottom slope may be indicative of active faulting and folding but need additional data for confirmation of the recency of activity. The core holes on the cross section indicate a westward thickening section of Pliocene to Recent sediment abutting the eastern strand of the SCOZD, and high-resolution seismic reflection data indicate minor deformation of the sediment on the southwest side of the fault strand. These data suggest that the eastern strand of the SCOZD has been active through the Pleistocene and possibly in recent time. However, for the aforementioned fold additional supporting data reflecting the latest age of folding are lacking.

The plan view on Plate 2-3 shows an enlarged plot of the contours of the "C" horizon (Plate 2-1) and the individual strands of the SCOZD that offset the " C" horizon. The "C" horizon as mapped by Western Geophysical is defined as the acoustic basement and probably represents more than one rock type. On the northeastern side of the SCOZD the acoustic basement is the top of the San Onofre Breccia. However, southwest of the SCOZD the acoustic basement has been classified as the Catalina schist. Within the SCOZD fault zone the acoustic basement is not well imaged, and identification of the reflector and associated rock type is uncertain.

The SCOZD in the depicted area consists of a band of several near-vertical strands (labeled A to D) of varying types and amounts of vertical offset. Only the northeastern strand (A) is interpreted to cut the mapped Miocene horizon (near top of Monterey formation). Strands B1 and B2 are not the same fault but represent short cross faults between A and C. Several strands (labeled C) that are separated on line WS-70-18 are closely spaced on line W-10. Horizontal offsets across the fault strands are not indicated on the vertical sections but have been inferred from the contour patterns of the mapped surfaces and other geological and seismological data.

A sub-horizontal reflector is annotated on the seismic reflection record of line W-10. This reflector corresponds (as nearly as can be determined from the available illustrations) to the detachment faults and thrust faults illustrated on Nekton line 49-102 from Crouch and Suppe (1993), the Oceanside detachment on USGS line 120 of Bohannon and Geist (1998), and the blind thrust of Fischer and Mills (1991) (Figures 2-9, 2-6, and 2-10 of this report). It also apparently corresponds to the Oceanside thrust fault of Rivero and Shaw (2000 and 2001) (Plate 2-2 and Figure 2-8). The image shown on line W-10 dips to the northeast from about 1.8 seconds at SP 192 to 3.2 seconds SP 80. This represents a dip of approximately 17 degrees between SP 192 and SP120 using the velocities shown on Plate 2-3. From SP 120 to SP 180 the apparent dip remains the same, but true dip increases to approximately 25 degrees due to the higher velocity in the basement rocks.

The detachment as drawn is not a continuous reflector but appears to have been offset in the vicinity of strand D and possibly by the southwestern-most strand of the group labeled C. However, the other vertical strands within the C group clearly do not offset the reflector. The intersection with the most recently active strand of the SCOZD, strand A, is not apparent on this record nor on any of the other seismic reflection records reviewed for this report. If the detachment should extend toward the coast beyond SP 80 at the estimated 25 degree dip in the basement rocks, it would be at a depth of approximately 7 km where it crosses the coastline.

As stated in the SONGS 2&3 FSAR, the apparent decrease in fault length and continuity of the SCOZD in the younger units is also similar to the NI. Major differences noted were the more gentle nature of the folds, and lack of any prominent fault scarps on the sea floor, despite the recognition of sea floor irregularities of uncertain origin. Interpretation of high resolution geophysical profiles indicate that the SCOZD intersects the sea floor locally; however the system is generally not overlain by Pleistocene and Holocene deposits except along the eastern (shoreward) edge of the zone.

Moore (1980) analyzed the available high-resolution seismic reflection data in the area between Dana Point and Oceanside, the area generally not covered by the deep seismic reflection data. He correlated these data with both the Western Geophysical data on the west and the bore hole paleontological data. The high-resolution data provide information in the nearshore zone between the SCOZD and the coastline. Moore's conclusions regarding faults east of the SCOZD (referred to as HOZD in his reference) were that they were of two types. First, he identified and mapped very old faults that cut the San Onofre

Breccia but did not extend very far into the older Monterey section. The second category of faults was recognized as interformational faults associated with folding. The latter group he noted did not extend deep into the section nor upward into the Pleistocene unconformity. He also concluded that the data did not reveal a seaward extension of the Cristianitos fault beyond about 6000 feet from the shoreline.

The RC is mapped in the offshore as a continuous fault trace in both acoustic basements (Horizon C) and upper Miocene (Horizon B) units that extends from La Jolla Cove north to the Oceanside area. Based on the north-south trend of the northern Rose Canyon fault trace and the igneous intrusions at the south end of the SCOZD, these two fault zones were determined (SONGS 2&3 FSAR) to be disassociated. Onshore the Rose Canyon fault zone is coincident with a sublinear north-northwest trending topographic depression from La Jolla Cove, south through Rose Canyon, along the east side of Mission Bay to San Diego Bay, where it appears to die out as a widening zone of short, principally dip-slip faults. Geologic data available in the early 1980's indicated that the RC has been active since at least early Pleistocene and has experienced post-late Pleistocene and possibly Holocene deformation. More recent paleoseismic investigations of a strand of the Rose Canyon fault in San Diego indicate that the fault has undergone dominantly right-slip displacement during the Holocene (Lindvall and others, 1990; Rockwell and others, 1991 and 1992). Based on evidence that indicate that 3 m of right slip occurred during the most recent event on the Rose Canyon fault, Dr. T. Rockwell (personal communication, September 25, 2001) concludes that this likely was a M7 or greater earthquake and that the fault must extend a significant distance offshore to the north to accommodate a rupture of this size.

Other investigators also have considered the SCOZD as part of a relatively continuous right lateral transpressional fault system (Figure 2-14). Crouch and Bachman (1989) noted that the linear trend of wrench-related fold and flower structures recognized in the offshore are similar in size and character to the faulted anticlinal structures along the Newport-Inglewood trend in the Los Angeles basin. Crouch and Suppe (1993) show the Newport-Inglewood fault and Rose Canyon faults as a continuous fault zone in the offshore (Figure 2-4). They suggest, however, that faults such as the Newport-Inglewood fault may have originated as high-angle, hanging wall normal faults above detachments and hence, modern strike-slip along these faults may end downward against the detachments. Legg and Kennedy (1991) note that vertical tectonics associated with divergent, right bends or fault offsets, and convergent, left bends or fault offsets, result in active pull-apart basins or push-ups along the major right-lateral zones. Legg (1991) shows the Newport-Inglewood fault as a continuous structure that subparallels and forms a stepover to the Rose Canyon fault in the offshore north of San Diego. He notes the transpressional structure along the offshore Newport-Inglewood fault zone and the prominent northwest-trending thrust faults as the base of the continental slope west of Newport and San Juan Capistrano, which suggest northeast-southwest convergence in this area.

Fischer and Mills (1991) and Fischer and Lee (1992) evaluated the location, segmentation, recency, and slip rate of faults within the SCOZD using high-resolution

and newer (1989) digitally processed seismic reflection data. They interpreted the structure of the fault zone to be a positive flower structure and concluded that the SCOZD is a part of the Newport-Inglewood-Rose Canyon fault zone. Segmentation arguments based on structural and geometric characteristics as well as evidence for recency of movement presented by Fischer and Mills (1991) were incorporated in the seismic source characterization model for the IPEEE seismic hazard study (Risk Engineering, 1995, Appendix A) (Figure 2-15).

Based on interpretation of high-resolution, multichannel seismic reflection data collected by the USGS in 1998 and 1999 and boomer data collected over the shelf and slope in 2000, scientists from the US Geological Survey (Sliter and others, 2001) interpret recent faulting at the base of the slope between Dana Point and Oceanside to be related to a strand of the NI. They note that the faults strands mapped on the shelf north of Oceanside, however, do not displace the seafloor. They conclude that the strand at the base of the slope may connect with the RC by a left step near Carlsbad, as evidenced by recent folding of the seafloor.

2.2.2 Relationship of the San Joaquin Hills Blind Fault to the Oceanside Blind Thrust

Geophysical data and interpretations of the structural framework of the offshore region adjacent to SONGS as outlined in the SONGS 2&3 FSAR and by Fischer and Mills (1991) also pertain to the continuity and structural relationship between onshore and offshore folds. As noted above in Section 2.1.1, Mueller and others (1998b) and Rivero and others (2000) infer that the postulated active fault-bend fold associated with the San Joaquin Hills is the onshore continuation of a fold imaged in offshore seismic data. The viability of this structural link has implications for the seismogenic potential of both the San Joaquin Hills blind fault (SJBF) and the Oceanside blind thrust (OBT).

Both onshore and offshore geologic data suggest that the continuity of the structural wedge backthrust between the San Joaquin Hills and offshore region as described by Mueller and others (1998b) and Rivero and others (2000) is not viable. These observations and inconsistencies are described below.

The San Joaquin Hills active fold as mapped by Mueller and others (1998b) and Grant and others (1999) extends well north of the projected onshore extension of the Oceanside detachment as mapped by Rivero and others (2000) (Plate 2-2). Thus, it is not clear that the active fault-bend fold assumed to underlie the San Joaquin Hills is in the hanging wall of the Oceanside blind thrust as implied by the structural wedge thrust model.

The doubly plunging folds as mapped by Mueller and others (1998b) and Rivero and others (Figure 2-2, Plate 2-2) suggest that the two folds are not directly linked.

The relationship of the active folds to older bedrock structure is different between the onshore San Joaquin Hills active fold and the offshore fold. The main bedrock structural feature in the San Joaquin Hills area is a complexly faulted, northerly plunging anticline

with the Capistrano syncline bordering it on the east (Vedder, 1975; Vedder and others, 1957; Morton and Miller, 1981). The axis of this north-trending asymmetric broad fold crosses the shoreline a few kilometers north of Dana Point (Figure 2-12). The axis of the Quaternary fold as mapped by Mueller and others (1998b) and Grant and others (1999) trends more northwesterly and cross cuts the pre-existing structural fabric.

Western Geophysical (1972) maps a major north-trending, structural high, named the Offshore San Joaquin Hills anticline, that appears to be the seaward extension of the onshore San Joaquin Hills anticline. Onlap of Upper Miocene rocks suggests that this acoustic-basement structural high, which is approximately 5 to 13 km wide (Plate 2), has been stable since Middle Miocene. Both the onshore and offshore structural highs are associated with a prominent, positive Bouguer-gravity anomaly. Fischer and Mills (1991) map the culmination of the westernmost crest of the offshore San Joaquin ridge south of the NI zone to be about 7 km west of the projection of the onshore San Joaquin high axis into the fault (Figure 2-12) and use this apparent offset as a measure of right-lateral slip on the NI-RC fault zone. Western Geophysical (1972) reports a possible lateral offset between the axes of only 2.1 km (7000 ft) and notes that this apparent offset may result from normal faulting that occurs on the upthrown (landward) side of the SCOZD. The breakaway zone of the Oceanside detachment as mapped by Rivero and others (2000) cuts diagonally across the offshore San Joaquin structural high (Plate 2-2).

The offshore fold that Mueller and others (1998b) and Rivero and others (2001) (Plate 2-2) interpret to be related to a west-dipping backthrust of an active structural wedge coincides with a prominent complex anticline or anticlinorium that has been inferred to represent a positive flower structure along the NI-SCOZD (Moore, 1980; Fischer and Mills, 1991). This complex anticline is prominently faulted in most, but not all, places (Moore, 1980). As illustrated in the series of 1978 high-resolution sparker profiles presented by Moore (1980, his Figure 14), this fold which is clearly imaged south of San Onofre appears to die out to the north in the vicinity of SONGS. In contrast to the interpretations presented by Western Geophysical (1972), Moore (1980), and Fischer and Mills (1991); Mueller and others (1998b) and Rivero and others (2000) (Figure 2-3, Plate 2-2) do not interpret a high angle strike-slip fault that displaces Upper Miocene strata at or near the sea floor. In contrast to the onshore San Joaquin Hills active uplift, the offshore fold subparallels older bedrock structure.

In summary, the link between the offshore fold that Rivero and others (2000) and Rivero and Shaw (2001) interpret to be the backthrust of a wedge thrust system and the postulated blind thrust underlying the San Joaquin Hills active uplift is, at present, not demonstrated by the available geologic and geophysical data.

2.3 SEISMIC SOURCE CHARACTERIZATION

Based on the recent research described in the previous section, Mueller and others (1998a and 1998b), Grant and others (1999), Rivero and others (2000), and Rivero and Shaw (2001), postulate that there may be blind fault sources in the vicinity of SONGS. These postulated blind faults were not explicitly modeled in the IPEEE hazard study (Risk

Engineering, 1995). A key factor in the assessment of these postulated blind faults and their impact on hazard at SONGS is the lack of knowledge regarding the structural relationships and interaction between them and the active strike-slip faults in the inner continental borderland. As noted above, various investigators have presented differing interpretations of the available geophysical and geological data.

Rivero and others (2000) propose four possible interactions between the two classes of faults (i.e., blind thrusts and strike-slip faults), each solution requiring a different fault geometry at depth that influences hazard estimates (Figure 2-16). In brief the four alternatives are:

A. Younger strike-slip faults cut and preclude further activity on older thrusts. Rivero and others (2000) consider this solution incompatible with the seismologic, geodetic, and geologic evidence supporting their interpretation of present activity on the thrust system.

B. Active thrusts terminate at strike-slip faults that extend through the entire seismogenic crust. Rivero and others (2000) state that this solution is plausible for the Oceanside thrust.

C. Active thrusts offset the strike-slip fault zones. This solution permits coeval activity on both types of faults and yields independent thrust and strike-slip fault sources.

D. The thrust and strike-slip faults may merge into a single structure at depth. Oblique slip on a deep fault is partitioned into pure thrust and strike-slip motion on the shallow faults.

For this study, we have developed three alternative source characterization models to capture the range of plausible fault source geometries and interactions that would have a significant impact on the seismic hazard to SONGS (Figure 2-16). Solution B as outlined by Rivero and others (2000) was not explicitly included in this study for the following reasons: In the vicinity of the SONGS, the Oceanside detachment intersects the high-angle strike slip fault (SCOZD as characterized previously) at an estimated depth of 5 to 6 km, above the depth where major earthquakes are expected to nucleate. As noted in the IPEEE study (Risk Engineering, 1995, Appendix A), localized reactivation of the shallow portion of the detachment to the west of the SCOZD or reverse faulting in proximity to the SCOZD may be explained by local strain partitioning (Lettis and Hanson, 1991) associated with a predominantly strike-slip fault (Figure 2-17). Also, the observation of coastal uplift used to demonstrate activity on the Oceanside blind thrust is not applicable for this solution given that the postulated active thrust does not extend beneath the coastline.

A general logic tree showing the three alternative source characterization models and resulting fault sources is shown in Figure 2-18. Figure 2-19 shows the logic tree used to characterize the Oceanside blind thrust (OBT) in Model 2. Maps of the fault sources

included in the three different alternative source models are shown on Figures 2-20, 2-21, and 2-22. A summary of the source parameters used to describe the seismic sources for each of these models is provided in Table 2-1 and discussed below.

The assessment of maximum magnitudes for strike slip and blind thrust fault sources characterized for this study follows the methodology used in Risk Engineering (1995, Appendix A). Maximum magnitude distributions were assessed using the rupture length distributions given in Table 2-1 and the empirical magnitude-rupture length and magnitude-rupture area relationships developed by Wells and Coppersmith (1994). Rupture areas were computed assuming that the full width of the seismogenic crust ruptures in the maximum event. Empirical relationships relating magnitude to subsurface length and magnitude to rupture area are given equal weight.

2.3.1 Model 1

This model assumes that the NI-SCOZD-RC is an active strike-slip fault zone that truncates and displaces the Oceanside detachment. In this model the characterization of the NI-SCOZD-RC fault zone follows that described in Risk Engineering (1995, Appendix A). In that characterization two segmentation scenarios were given equal weight. Model 1-A assumes that the onshore NI and the SCOZD are part of the same fault zone, and that ruptures may propagate across the small stepover between the two faults. The more major 2.5 to 4.5-km-wide Carlsbad-Encinitas stepover between the southern segment of the SCOZD and the RC fault as defined by Fischer and Mills (1991) is assumed to act as a barrier to surface ruptures, and, therefore, the two faults are considered independent sources. Model 1-B assumes that the onshore segment of the NI is an independent fault source that is characterized by a lower rate of activity. In this alternative, the SCOZD-RC fault zone is considered to be a single fault zone as interpreted by Fischer and Mills (1991) and Fischer and Lee (1992).

The Oceanside detachment is not considered to be an active seismogenic source, and a NE-vergent blind fault underlying the San Joaquin Hills is modeled as a potentially active fault that merges with or is truncated by the NI-SCOZD-RC fault zone at depth. The seismogenic potential of the San Joaquin Hills blind fault (SJBF) is not known. The geometry and location of the blind fault inferred to underlie the San Joaquin Hills are not well constrained. The SJBF could be linked directly with the NI, such that movement on the SJBF occurs during slip events on the NI (i.e., local strain partitioning as defined by Lettis and Hanson, 1991) (Figure 2-17). Alternatively, the SJBF could operate as an independent blind thrust or reverse fault that accommodates a component of convergence in the present transpressional tectonic environment (i.e., regional strain partitioning as defined by Lettis and Hanson, 1991). Due to the uncertainty in the geometry (depth and dip) of the San Joaquin Hills blind fault and its relationship to the Newport-Inglewood fault zone offshore, a probability of 0.5 is assigned to the likelihood that this fault is an independent fault source.

The total length of the San Joaquin Hills blind fault is based on the total length of the fold as shown by Mueller and others (1998b). Rupture lengths of 25 and 37 km are considered

with higher weight (0.7) given to the portion of the fold that is best expressed geomorphically. The buried fault is modeled as a SW-dipping fault plane. The location of the tip, which is conservatively assumed to be at a depth of 1 km, is defined by the eastward extent of the fold. The fault is assumed to intersect the Newport Inglewood fault at depths of greater than 5 km to the base of the seismogenic crust (12 or 15 km). The following range of dips are included in the model: 30°W (0.3), 40°W (0.4), and 50°W (0.3).

Slip rate estimates are based on the distribution used for fault dip and the late Pleistocene uplift of the San Joaquin Hills as indicated by the elevated marine terraces. The slip rates on the fault plane were obtained by dividing the local uplift rates listed in Table 2-1 by the sine of the fault dip angle. It was assumed that some of the late Pleistocene uplift observed in the San Joaquin Hills is due to regional uplift as evidenced by the relatively uniform coastal uplift of 0.1 to 0.17 mm/yr south of Dana Point to San Diego. Thus, the late Pleistocene uplift rate of 0.21 to 0.27 mm/yr recorded by marine terraces in the San Joaquin Hills (Grant and others, 1999) was reduced by 0.1 mm/yr to calculate a local uplift rate that could be used to evaluate a slip rate for the San Joaquin Hills blind fault.

Maximum magnitude distribution plots for the fault sources included in Model 1 (NI-SCOZD (Model 1-A), RC (Model 1-A), SCOZD-RC (Model 1-B), NI (Model 1-B), and SJBF) are shown on Figure 2-23.

2.3.2 Model 2

Model 2 allows for independent active strike-slip and blind thrust faults to be present in the inner continental borderland adjacent to SONGS. This model includes an active Oceanside blind thrust (OBT) as well as independent strike-slip faults, the NI to the north and the RC to the south (Figures 2-21). A logic tree outlining the characterization of the OBT in this model is shown in Figure 2-19. This model does not explicitly model a displaced strike-slip fault as shown in Solution C of Rivero and others (2000). Rivero and others (2000; personal communication, September 24, 2001) do not show a strike-slip fault in the hanging wall of the Oceanside blind thrust (OBT) in the vicinity of SONGS (Figure 2-3A, Plate 2-2). Rather, the en echelon folds inferred by others (e.g., Moore, 1980; SONGS 2&3 FSAR; Fischer and Mills, 1991) to be related to transpression along a predominantly strike-slip fault (SCOZD) are judged by Rivero and others (2000) to be due to a backthrust in a wedge thrust structure. The wedge thrust interpretation implies that there is not a continuous strike-slip fault connecting the Rose Canyon (RC) and Newport-Inglewood (NI) faults. Crouch and Suppe (1993) do interpret a high-angle strike-slip NI on line 49-102 in the offshore north of SONGS (Figure 2-9); however, they suggest that the fault may have developed as a high-angle, hanging-wall normal fault above the detachment and hence, modern strike-slip may end downward against the detachment. This would limit the strike-slip fault (SCOZD) to the upper 5-6 km in the vicinity of SONGS. In this interpretation, the strike-slip fault would not extend to earthquake nucleation depths for large and moderate earthquakes and thus there would be little or no moment release occurring along this portion of the SCOZD during strike-slip earthquakes nucleating on either the adjacent NI or RC. These observations, while not

inconsistent with the co-existence of the OBT and strike-slip faults, do not support the offset strike-slip geometry as shown in Solution C (Rivero and others, 2000).

The characterization of the NI and the RC faults, which for Model 2 do not include the SCOZD, follows Risk Engineering (1995, Appendix A). The NI north of the OBT is modeled as a strike-slip fault to seismogenic depth. The RC, like the SCOZD, lies in the hanging wall of the OBT. However, the RC, unlike the SCOZD, likely extends as a near-vertical strike-slip fault to seismogenic depth. The intersection of the southern OBT and the RC, the location of which is a function of the steeper dip of the southern OBT and distance between the breakaway zone for the OBT and the RC, lies at or near the base of the seismogenic crust.

The location and geometry of the OBT follows Rivero and others (2000; written communication, September 28, 2001). There is no direct evidence to demonstrate the presence of an active blind thrust beneath SONGS. The location and dip of the postulated OBT east of the SCOZD is not imaged in seismic data.

As outlined in Figures 2-18 and 2-19, alternative fault lengths are considered for the OBT depending on whether or not the San Joaquin Hills blind fault (SJBF) is judged to be structurally linked to the OBT and if the OBT is segmented. If the SJBF is modeled as a backthrust forming a wedge structure with the OBT (i.e., linked), it is not considered as an independent seismic source because it intersects the OBT at a depth of 5 km (i.e., does not extend to seismogenic depth). In this case the OBT is extended north to Newport Beach (OBT-long) resulting in a shorter NI (NI-short). When the SJBF is not linked with the OBT, the NI is extended to south of Dana Point (NI-long) and the SJBF is considered an independent seismogenic source that is bounded on the west by the NI. Based on the geologic and structural observations outlined in Section 2.2.2, we assign a weight of 0.2 to the branch in which the SJBF is directly linked to the OBT as a backthrust and a higher weight (0.8) to the unlinked branch.

Several geometric and structural observations suggest that the OBT can be subdivided into two distinct segments, a northern and southern segment. The boundary between the two lies approximately at the latitude of 33°N. Geometrically, there is a change in fault dip across this boundary with the northern segment exhibiting a significantly lower dip angle (~14°) relative to the southern segment having a dip angle of (~24°). Coincident with this general change in dip, there is a distinct bend (offset) in the location of the breakaway along the strike of the OBT. Based on the location of the 5 km depth contour on the OBT (Figure 2-11) and the dip of the thrust plane, the depth of the western (updip) extent of the blind thrust appears to be greater (2.8 km) along the northern segment versus the depth (1.4 km) of the tip for the southern segment.

Structurally, the northern segment is associated with more pronounced and probably more recently active hanging wall fold deformation. In addition to the backthrust associated with the thrust wedge mapped in the offshore south of Dana Point (Plate 2-2), the San Mateo thrust and Carlsbad thrusts are recognized post-Miocene contractional structures in the hanging wall of the northern OBT (Rivero and Shaw, 2001; Plate 2-2).

In contrast, only a limited zone of active folding, localized along the breakaway zone, is indicated for the southern segment (Plate 2-2).

Rivero and others (2000) show the OBT as a continuous structure in the inner continental borderland from near Newport Beach south to near the Mexico-United States international border (Figure 2-7). Based on the continuity and evidence for late Pleistocene coastal uplift along the entire structure, they conclude that the full length of the thrust could rupture in an event and use these fault dimensions to estimate maximum magnitudes of Mw 7.3 (restricted to west of the NI-RC) and Mw 7.5. They allow that the OBT could rupture in smaller events, but note that direct evidence for segmentation of the thrust is not apparent. Rivero and Shaw (personal communication, September 24, 1997) acknowledge that the geological and structural observations listed above, support segmentation of the OBT. Based on these observations, we could conclude that a rupture of the entire OBT is unlikely. However, in the absence of behavioral data that preclude such events, an unsegmented OBT rupture is included in the source characterization model with relatively low weight (0.05).

The possibility that the maximum magnitude earthquake that may occur on the OBT will not rupture the entire fault is included in the assessment of the segmented OBT. For OBT (N)(long) where the SJBF is linked with the OBT, three maximum rupture scenarios are considered: 82 km (the total length of the segment); 51 km (the length of the structure identified in offshore seismic data); and 36 km (the length of the active wedge thrust in the offshore as indicated by the fold geometry associated with the backthrust. The arguments cited above for not linking the offshore and onshore folds also apply to the weighting of a full segment rupture. The highest weight is given to the 51 km rupture length scenario (0.6), with lesser weight (0.2) given to both the longer and shorter rupture scenarios. For the OBT (N) (short), the total length of the segment (51 km) and the 36 km (the length of the active wedge thrust) are given weights of 0.6 and 0.4, respectively. Two rupture length scenarios are considered for the OBT (S): 49 km (the total length of the segment); and 36 km. These are assigned weights of 0.6 and 0.4, respectively.

Maximum magnitude distributions for each of the alternative OBT fault sources are shown on Figure 2-23. Uncertainty in the choice of maximum rupture length and the downdip extent (calculated from fault dip and the depth of the seismogenic crust) (Figure 2-19) are reflected in the assessment of the maximum magnitude distributions.

As summarized in Section 2.1.2, three different approaches have been used by Rivero and others (2000; written communication, October 16, 2001) to estimate the slip rate for the OBT. The estimated slip rates reflect average rates of activity over three different time periods: (1) long-term average post-Pliocene (~3.6 Ma) rate of 0.8 to 1.0 mm/yr based on structural analysis of fault-fold relationships; (2) post-late Pleistocene (~125 ka) rate of 0.23 to 0.41 mm/yr calculated from marine terrace uplift rates assuming a wedge thrust structural model; and (3) current rates based on analysis of geodetic data (maximum rate of 2.2 mm/yr based on a rate of convergence inferred by Kier and Mueller, 1999).

The slip rate distribution used to characterize the OBT for this study captures the full range of slip rates calculated using these alternative approaches. The values and weights assigned to them are: 0.25 mm/yr (0.2), 0.4 mm/yr (0.45), 1.0 mm/yr (0.3), and 2.2 mm/yr (0.05). The highest value (2.2 mm/yr) is given low weight based on the more comprehensive analysis of geodetic data (Section 3.0) that indicates that there is little or no measurable convergence occurring across the OBT. The highest weight is given to the long-term average rate inferred from uplifted marine terraces. Assuming that this uplift is due to displacement on the OBT, the relatively well constrained age and elevation of the late Pleistocene stage 5e marine terrace along the coast provides the best indication of long term deformation rates in the current tectonic environment. Rivero and others (2000) note that the rates inferred from the coastal uplift are minimum values in that long term uplift may be affected by isostatic compensation and/or flexural subsidence that may occur due to crustal thickening. These factors, which may be significant in the deeper Los Angeles Basin, likely are not a major consideration in the inner borderlands in the vicinity of SONGS. The long term post-Pliocene rate reflects the average slip rate since inception of folding in the inner borderland (~3.6 Ma). This long term rate is higher than the rate inferred from the marine terrace uplift. Elsewhere in the Los Angeles Basin, long term post-Pliocene rates for contractional structures (e.g., the Compton thrust) are significantly higher than would be suggested by Quaternary deformation. For example, Shaw and Suppe (1996) assumed a long term (post-2.5 Ma) average slip rate of 1.4 ± 0.4 mm/yr for the Compton thrust. Subsequent Quaternary studies by Mueller (1997) indicate that during the past 300 ka the Compton thrust has been inactive or has had a very low slip rate. Due to uncertainties in the timing and history of contractional deformation in the hanging wall of the OBT, the higher slip rate inferred from the post-Pliocene fold analysis is judged less indicative of the current rate of slip than the rate estimated from the uplifted late Pleistocene marine terraces.

2.3.3 Model 3

In this model, the OBT and SCOZD-RC represent strain partitioning in the upper crust above an oblique fault plane at depth (Alternative D, Rivero and others, 2000). A simplified fault plane based on the location and dip (14°) of the northern segment of the Oceanside blind thrust as provided by Rivero (written communication, September 28, 2001) is used to model the fault source in the vicinity of SONGS. Following Rivero and others (2000) a maximum magnitude of MW =7.6 is used. In addition to the range of slip rate values (1.19 to 2.91) given by Rivero and others (2000) for an oblique slip fault, an intermediate slip rate value of 1.7 mm/yr (calculated from the weighted average strike-slip and dip slip rates for the RC and OBT, respectively) is used. The direction of slip in the plane of the fault at depth is dependent on the ratio of dip slip versus strike slip. For this sensitivity analysis, the mean rake angle of 22° calculated using the weighted average values for strike-slip and convergence is used to model the direction of slip on the oblique thrust fault at depth.

Examination of empirical data for historical earthquakes worldwide suggests that oblique slip events on shallow dipping fault planes do not occur or are extremely rare. Wells and

Coppersmith (1991; PG&E, 1990) examined the relationship between fault dip and sense of slip (expressed as the rake angle) for about 170 earthquakes worldwide having published focal mechanisms. The rakes were based primarily on focal mechanisms derived from waveform inversion. Fault dips were estimated primarily from focal mechanisms and the geometry of aftershocks, and to a lesser extent from surface exposures of the fault plane that ruptured. The relationship between coseismic fault dip and rake angle is shown on Figure 2-24. The data show very few shallow dipping earthquakes, and these all have rake angles of greater than 50 degrees. Given the inferred dip angle of the OBT (14° to 24°), it is not likely that this fault would accommodate a significant component of strike-slip. The weighted average values of strike slip (partitioned updip onto the Rose Canyon fault) to dip slip (partitioned updip onto the OBT) suggest a mean rake angle of 22° for the Oceanside oblique fault at depth. Oblique slip likely would be accommodated on a more steeply dipping fault, but as noted previously there is no geologic evidence to suggest a steepening of the detachment beyond the eastern limit as imaged in seismic data. This model, therefore, is given very little weight as a viable source characterization model.

2.3.4 Weighting of Alternative Models

The weights assigned to the three alternative source models that characterize the postulated blind thrust faults that would pose significant hazard to SONGS (i.e., the OBT and SJBF) are based on consideration of the evidence for the activity and seismogenic potential of these faults, as well as geologic and geodetic evidence that pertain to the style and rate of deformation that is occurring in the present tectonic environment.

The Oceanside detachment appears viable as an east-northeast-dipping basement/cover contact in the inner California borderland in the vicinity of SONGS, but there is no direct evidence that clearly demonstrates the activity and seismogenic capability of the Oceanside Blind thrust (OBT) as postulated by Rivero and others (2000). Evidence presented by Rivero and others (2000) regarding the level of activity, slip rate, and seismogenic potential of the OBT as a source of future large magnitude earthquakes is inconclusive.

We give some weight to the possibility that the OBT may be a capable seismic source for the following reasons: The wedge/thrust model developed by Rivero and others (2000) and Rivero and Shaw (2001) to explain recent fold deformation along the offshore zone of deformation (SCOZD) is based on a systematic analysis and review of an extensive set of seismic data. This model may provide an alternative explanation of the apparent discontinuity of post-Upper Miocene faulting along the SCOZD. Seismic data do not image the intersection of the postulated Oceanside detachment and the high-angle strike slip faults mapped by others along the SCOZD, thereby making it difficult to demonstrate that the OBT does not displace strike-slip faults along the NI/SCOZD/RC trend or that a strike slip fault along the SCOZD extends to seismogenic depth.

The activity and seismogenic potential of the OBT is less definitive. The evidence cited by Rivero and others (2000) and Rivero and Shaw (2001) is based on (1) geodetic

measurement of contractional crustal strain, (2) regional coastal uplift; (3) geophysical evidence of post-Pliocene folding in the offshore region; (4) a structural relationship between the San Joaquin Hills and a similar wedge/thrust structure in the offshore; and (5) association of the 1986 Oceanside earthquake with a component of the Inner California thrust belt system (the Thirtymile Bank blind thrust). Each of these lines of evidence may have some viability for indicating the seismogenic capability of the OBT, but as noted below they are also consistent with a predominantly strike-slip regime.

A much stronger case is made in support of the model that characterizes the SCOZD as part of a through-going strike-slip fault zone. The chief arguments supporting the higher weight given to the strike-slip model (Model 1) are:

- Previous interpretations of 2D and high-resolution shallow seismic data show evidence for a relatively continuous zone of deformation linking the RC and NI (Western Geophysical, 1972; Fischer and Mills, 1991; Crouch and Suppe, 1993).

- Seismicity and paleoseismic data show that the Newport-Inglewood (NI) and Rose Canyon (RC) faults are capable strike-slip faults (Hauksson and Gross, 1991; Rockwell and others, 1991 and 1992).

- Evaluation of recently acquired high-resolution seismic data by the USGS supports connection of the NI and RC faults along a recently active strand at the base of the continental slope (Sliter and others, 2001).

- Geodetic data show that strain in the southern Californian inner borderland is characterized by north-northwest directed shear subparallel to the overall North America/Pacific plate motion. Little or no convergence across the inner borderland normal to the plate boundary in the vicinity of SONGS is indicated (Section 3.0). In particular, the lack of significant convergence in the regional signal to the east of the OBT suggests there is not a regional "driving" force that would reactivate a large seismogenic thrust.

- Fault and fold deformation observed along the SCOZD is consistent with transpressional right lateral slip along a N20°W trending fault.

- Evidence to support reactivation of the entire OBT in the current tectonic environment is not demonstrated. Seismicity (1986 Oceanside earthquake) and possible late Pleistocene/Holocene faults and associated folding can be explained by localized reactivation (strain partitioning) and contraction in left steps or bends in a transpressional right-slip tectonic environment.

- Clockwise rotation of crustal blocks in the inner borderland, which is not inconsistent with geodetic data that suggests a component of extension cross the southern inner borderland (see Section 3.0), could account for the greater intensity of contractional structures in the hanging wall of the northern OBT

west of the SCOZD. This might explain the local reactivation of portions of the OBT, but would not require reactivation or rupture of the entire detachment.

- Much of the contractional deformation observed in the inner borderland (e.g., the San Mateo thrust belt and the Carlsbad thrust) could have occurred during the Pliocene within a different stress regime. Based on geologic evidence that suggests coastal uplift in the San Diego region as well as activity on the Elsinore fault were initiated approximately 0.9 to 1.0 Ma, Dr. T. Rockwell speculates that a reorientation of the plate vector may have occurred in the region during early to middle Quaternary time (personal communication, September 25, 2001). Evidence for inactivity or decreasing Quaternary slip rates compared to longer-term rates for blind thrusts in the Los Angeles basin (e.g., the Compton-Los Alamitos and Las Cienegas faults) (Ponti, 2001) also suggests a change in the tectonic stress regime.

- The initiation of thrusting in the offshore, which is inferred to have begun in the Pliocene (Crouch and Suppe, 1993; Rivero and others, 2000; and Rivero and Shaw, 2001), may significantly predate the initiation of coastal uplift as noted above. This would suggest that coastal uplift is not directly linked with movement on the Inner California borderlands thrust system. However, as noted by Rivero (personal communication, September 24, 2001), age estimates and correlation of stratigraphy across the fold belts in the offshore is not well constrained due to the paucity of offshore well control and the initiation of folding could have been later than previously estimated.

- Regional coastal uplift, which is cited by Rivero and others (2000) to indicate that the Oceanside and Thirtymile Bank thrusts are active over a region larger than the San Joaquin Hills, may be attributed to a large degree to other processes (e.g., rift shoulder thermal isostasy). Ongoing studies by Kier and others (2001, in review) suggest that the uniform regional uplift observed in southern California may reflect the far-field effect of unloading and rift shoulder development associated with lithospheric thinning in the northern Gulf of California and the Salton Trough (Kier and Mueller, 1999; Kier and others, in review). The Oceanside fault, as mapped south of the International border, does not extend far enough south to explain the regional coastal uplift observed well into Baja California.

- There is no marked change in the pattern of coastal uplift across the segmentation boundary between the more shallow dipping northern OBT and the steeper dipping southern OBT. This suggests that either the coastal uplift is not directly linked to slip on the OBT, or the southern segment has a lower slip rate. Dr. T. Rockwell notes that there is no evidence for tilting or significant differential uplift along the coast as recorded by the Quaternary marine terraces and underlying Tertiary bedrock (T. Rockwell, personal communication, September 25, 2001; Kier and others, in review).

Based on these observations, we assign the highest weight (0.7) to the source characterization model that includes a through-going NI-SCOZD-RC strike-slip fault system in the inner borderland adjacent to SONGS. Models 2 and 3, which both assume that the Oceanside detachment, which appears to have been reactivated at least locally as a low-angle thrust fault during the Pliocene, is currently active and seismogenic as a regional scale blind thrust in the present tectonic environment, are judged less likely. The remaining weight (0.3) is divided between these two options, with most of the weight (0.25) assigned to Model 2. There is little empirical evidence to suggest that oblique slip with the ratio of strike-slip to dip-slip suggested by the available data for the OBT would occur on a fault plane dipping between 14° to 24°. Therefore, the oblique OBT model is given very low weight (0.05).

3.0 EVALUATION OF GLOBAL POSITIONING SYSTEM DATA

In this section recorded tectonic ground displacement rates from the Global Positioning System (GPS) stations in southern California are systematically used to assess implications of the postulated Oceanside blind thrust (OBT). This systematic use of GPS data provides a check on the overall reasonableness of the postulated OBT and weights assigned to the different seismic source characterization models (Model 1, Model 2, and Model 3) in Section 2.0.

The following parts of Section 3.0 provide the methodology used in the assessment and the results of the assessment. The methodology section also provides some background considerations regarding GPS and the use of GPS in evaluating the reasonableness of postulated faults.

3.1 METHODOLOGY

The GPS is a system to locate the three-dimensional position of a point on or near the earth's surface and consists of the following three components:

1. 24 GPS satellites orbiting the earth
2. Receiver stations, which, in this case, are "stationary" and anchored in the ground
3. Control and data processing

In GPS a receiver station measures the distance between the station and accessible GPS satellites using the travel time of radio signals between the station and the satellites. The resulting distances, after corrected for signal delays through atmosphere and other considerations, are used in triangulation to record the location of the receiving station as a function of time. Accurate timing for receiver stations through the use of an extra (fourth) satellite and knowing with precision where the satellites are in space contribute to the adequately accurate recorded location of the station.

For stationary stations, the error associated with a standard GPS could be as low as on the order of less than several meters since the government stopped scrambling the GPS signals. In addition, differential GPS makes differential corrections to take some delay bias out, thus reducing the error to less than a meter and sometimes in the centimeters range. Repeated measurements and other refinements further reduce the error range to millimeters for those GPS stations being used for measurements of tectonic ground displacements.

Some general considerations on GPS can be obtained under the following URL's:

- http://www.trimble.com/gps/index.html
- http://www.scign.org/
- http://users.erols.com/dmilbert/accur.htm

3.1.1 Sources of GPS Data in Southern California

For tectonic ground displacement data based on GPS, southern California is fortunate because the following two sources, together with their URL for the Internet access, exist:

- Southern California Integrated GPS Network (SCIGN).
  - http://pasadena.wr.usgs.gov/scign/Analysis/index.html
- GPS Data for the SCEC Crustal Motion Mapping Effort (Version 2, 1998)
  - http://www.scecdc.scec.org/group_e/release.v2/

Figure 3-1 shows the SCIGN GPS receiver locations in the part of the southern California area shown. A star on Figure 3-1 indicates the SONGS site, and four alphanumeric characters provided next to each receiver station identifies that receiver station (for example, a station closest to the SONGS site is identified by SCMS). Figure 3-1 also shows a composite geometry of Model 2 and Model 3 as well as parts of Model 1 for ease of reference. The SCIGN GPS sites are continuously monitored with the data updated daily and made available through the Internet.

Figure 3-2 shows the locations of the "general set" of SCIGN GPS receiver stations used in this study. The general set of SCIGN GPS stations consists of all stations that are in the general region of the SONGS site without regard to their potential appropriateness for the current study. However, as indicated on Figure 3-2, an attempt was made to include only those stations that are separated from the SONGS site by as few intervening seismic sources as possible, other than the seismic source(s) of interest. Therefore, for example, GPS stations east of the Elsinore fault were not included.

As discussed in Section 3.2, the general set of GPS stations shown on Figure 3-2 was used only to evaluate the general pattern of the tectonic ground displacement rates in the region surrounding the SONGS site. A selected set of GPS stations shown on Figure 3-2, which are considered more appropriate for this study (as discussed in Section 3.1.5), was used to evaluate the "total" and "incremental" displacement rates as discussed in Sections 3.3 and 3.4, respectively.

Figure 3-3 shows the locations of GPS receiver stations associated with the SCEC crustal mapping effort from the version 2 report dated 1998. The data set for the SCEC crustal mapping is being updated for the version 3 report, but that report and data are not yet released. The SCEC data set includes a GPS station site located adjacent to the SONGS site ("0301_GPS" on Figure 3-3, latitude: 33.37480 degrees north; longitude: 242.43519 degrees or 117.56481 degrees west) on a terrace deposit. This station, located within 200 feet of the State Parks Toll Booth, adjacent to SONGS Parking Lot #4, is just a monument and unfortunately is not a part of SCIGN and cannot provide a continuous recording of its location.

The GPS data set from the SCEC crustal mapping effort should be a superset of the SCIGN GPS data set because the SCEC crustal mapping efforts in general include GPS data outside of SCIGN as well as the SCIGN GPS data. However, the available SCEC

GPS data set from version 2 is not a superset. This is because the available SCEC GPS data set is dated 1998, and SCIGN GPS stations not listed in the 1998 SCEC GPS stations were added to SCIGN since 1998.

3.1.2 Relative Displacement Rates

Figure 3-4 shows the tectonic environment of California. The North American plate is moving southeast relative to the Pacific plate. The general tectonic movement of these two plates causes the majority of seismic activities in southern California. On Figure 3-4 the relative displacement rate vector (relative displacement vector over a one year period) of the point B with respect to the point A results when the displacement rate vector at point A is subtracted from the displacement rate vector at point B. The resulting relative displacement rate vector can be schematically represented by the vector shown on Figure 3-4 at the point B pointing toward southeast. Conversely, the vector shown at point A pointing toward northwest schematically represents the relative displacement rate vector of the point A with respect to the point B. For ease of reference, the term "vector" is often dropped when referring to displacement rate vectors or relative displacement rate vectors, but they should be considered as vectors.

Figure 3-5 shows the relative displacement rate of the SCIGN GPS receiver station called OGHS with respect to the SCIGN GPS receiver station called CAT1. The end of the relative displacement rate vector is placed at the OGHS station, and an error ellipse (Section 3.1.4), which in this case is quite small, is shown at the tip of the vector. The general sense of the relative displacement rate vector is similar to the one shown on Figure 3-4 at the point B. Many of the relative displacement rates shown in the following sections are similar to that shown on Figure 3-5 because in many cases the SCIGN GPS station CAT1 is used as the reference GPS point.

3.1.3 Simplified Tectonic Processes

In evaluating GPS data with respect to nearby postulated faults, it is useful to keep in mind some general relative displacement fields that likely would be expected based on very simplified and idealized tectonic processes associated with faults.

Figures 3-6a and 3-6b schematically show a simplified tectonic process associated with a strike-slip fault in terms of a perspective view and a plan view. As indicated on the perspective view of Figure 3-6a, the strike-slip fault is locked along the heavy dashed line within the "elastic" (seismogenic) zone with some tectonic forces in the "plastic" (or "creeping") zone at some depth, tending to "load" or "drive" the left side of the fault into and the right side of the fault out of the perspective plane of the figure. The resulting field of idealized relative displacement rates along the line connecting the points B's and A with respect to the point A schematically may be that shown on the plan views of Figures 3-6a and 3-6b.

Figures 3-7a and 3-7b schematically show a simplified tectonic process associated with a thrust fault (which could be a blind thrust), again in terms of a perspective view and a

plan view. As indicated on the perspective view of Figure 3-7a, the thrust fault is locked along the heavy dashed line within the elastic (seismogenic) zone with some tectonic forces in the plastic (or creeping) zone at some depth, tending to load or drive the hanging-wall side (right side of the fault on Figure 3-7a) of the fault into the foot-wall side (left side of the fault on Figure 3-7a) of the fault. (Note on the plan-view on Figure 3-7a, the direction of the relative displacement vectors, as indicated on Figure 3-7a, should point perpendicular to the strike of the fault; the variation of the lines pointing downward shown on Figure 3-7a indicates the magnitude variation only and not the direction of the relative displacement rate vectors.) The resulting field of idealized relative displacement rates along the line between the points B's and A with respect to the point A schematically may be that shown on the plan view of Figure 3-7b.

As can be seen in the schematic plots of Figures 3-6b and 3-7b, relative displacement rates at some distance away from the postulated faults need to be evaluated because only those rates appropriately reflect the tectonic ground displacement rates associated with the faults. In particular, for thrust (or blind thrust) faults, to the extent possible, the relative displacement fields some distance behind the hanging wall side ("behind" the fault) should be evaluated for tectonic ground displacement rates as reflecting the "loading" or "driving" force for the thrust fault. For the same reasons, the reference GPS stations also should be some distance away from the fault.

Some additional considerations regarding the mechanics of faults are provided at http://quake.wr.usgs.gov/research/deformation/modeling/index.html.

3.1.4 Error Ellipses

Figure 3-8a shows the two horizontal recorded displacement components (along the north or longitude direction and the east or latitude direction) versus time for the SCIGN GPS station CAT1, whose location is shown on Figure 3-5. Although the data shown on Figure 3-8a are filtered data, because of the "random error" the recorded data appear as two "thick" lines. The slopes of these thick lines correspond to the north and east components of the displacement rates. As shown on Figure 3-8a, these slopes are reported with ± error values.

Thus, for the north component, the slope and the error may be presented in the form: $\text{slope}_a \pm a$; similarly, for the east component, $\text{slope}_b \pm b$. These component slope and error values can be put in a vector form with error ranges as shown on Figure 3-8b, which can be viewed as a vector and an associated error ellipse as shown on Figure 3-8c.

The error ellipse shown on Figure 3-8c can be viewed as the "reported" error ellipse associated with that displacement rate. However, there may be other sources of errors, "systematic" or "random," which may be affecting displacement rates as reflecting the tectonic ground displacements. One such error source with a strong expected systematic component is the ground movements potentially induced by seasonal pumping of groundwater. One SCIGN GPS station FVPK near the SONGS site is reported (Bawden et al., 2001) to exhibit such an error. The recorded GPS displacement values for this site,

which are shown on Figure 3-9, show a very strong seasonal fluctuation of one of the horizontal displacement components, which correlates with a similar fluctuation of the vertical ("Up") component.

Another item that should be considered in evaluating GPS data is the duration of the GPS measurements. Two sets of SCIGN GPS stations and associated measurements are shown on Figure 3-10. As can be seen on Figure 3-10, the upper set (CAT1 and TRAK) shows relatively long measurement durations (more than six years) while the lower sets (CAT2 and SBCC) show relatively short measurement durations (a bit more than one year). In general, displacement rates from those with longer measurement durations should be more reliable than those with shorter measurement durations.

As discussed in Section 3.1.2, the GPS data in general are evaluated in terms of relative displacement rates in this study, which involve subtracting one displacement rate vector from another displacement rate vector. An upper bound estimate of error associated with such a difference is the sum of the errors associated with the minuend and subtrahend rates. Thus, the error ellipse associated with relative displacement rates would be higher than those associated with an individual displacement rate. Figure 3-11 schematically illustrates this increase of error ellipse. Figure 3-11 also shows an even larger error "ellipse" indicating reliability levels for the relative displacement rate vector that may reflect the "unreported" errors such as those described in Figures 3-9 and 3-10.

The error ellipses presented on figures herein for relative displacement rates correspond to the "reported" error ellipses (the one identified as "Error Ellipse A-B" on Figure 3-11). Thus, all the error ellipses presented herein should be viewed as lower bound ellipses in spite of how the reported error ellipses were calculated for relative displacement rates.

3.1.5 Selection of GPS Sites

For the GPS data set from the SCEC crustal map effort, all the GPS locations in the general region of the SONGS site as reported in the version 2 report were used to address only the overall pattern of relative displacement rates in the region. The usage of this GPS data set in this manner was considered appropriate because this data set was dated 1998 and is not current.

On the other hand, the SCIGN GPS stations have up-to-date GPS data that may be used for more detailed evaluations. However, some of these SCIGN GPS stations may not be appropriate for detailed evaluations for such reasons discussed in Sections 3.1.3 and 3.1.4. Therefore, the SCIGN GPS stations listed on Figure 3-2 were evaluated to select those SCIGN GPS stations that may be appropriate for further evaluations. Table 3-1 lists the SCIGN GPS stations listed on Figure 3-2 together with some considerations regarding each station. On the basis of considerations listed in Table 3-1, five SCIGN GPS locations indicated in Table 3-1 were selected: CAT1, MONP, NSSS, OGHS, and TRAK. Some of the key considerations used in the selection are as follows:

- Stations having adequate durations of records.

- Stations located adequately behind the hanging wall side of the postulated blind thrust fault ("behind OBT"), but not so far behind that other faults lie between the GPS station and the postulated blind thrust fault.

- Stations not affected by non-tectonic ground displacements such as those due to ground water pumping, which causes seasonal fluctuations.

- A pair of stations that when connected by a straight-line segment would intersect some significant part of the three postulated key faults: Model 1, Model 2, and Model 3.

These 5 SCIGN GPS stations, shown on Figure 3-12, were used to form four pairs of SCIGN GPS stations: CAT1-TRAK; CAT1-OGHS, CAT1-MONP, and CAT1-NSSS. On Figure 3-12, straight-dashed-line segments are drawn between these 4 pairs of GPS stations. As can be seen from Figure 3-12, the straight-dashed-line segments connecting these 4 selected pairs of GPS stations cross the postulated Model 1, Model 2, or Model 3 faults, involving NI-OZD-RC and OBT. Also, note on Figure 3-12 that these straight-dashed-line segments also go across the Palos Verdes / Coronado Bank fault system.

3.1.6 Relative Displacement Rates and Slip Rates

For detailed evaluations of selected SCIGN GPS station data, relative displacement rates from the GPS data are compared with geologically estimated slip rates associated with postulated seismic faults as schematically illustrated on Figures 3-13 and 3-14.

On Figure 3-13 a straight-line segment connecting point A and point B intersects a right-lateral strike slip fault. The relative displacement rate vector of point B with respect to point A based on GPS data is shown as a downward vector at point B. The solid downward vector on the right side of the strike slip fault corresponds to the geologically estimated slip rate associated with that fault. Note that this slip rate vector is about the same as the relative displacement rate vector at point B both in terms of direction and magnitude. This fact indicates that in this schematic figure the postulated fault and its geologically estimated slip rate are consistent with the GPS data. This means that the accumulated strain due to tectonic movement would be released by the slip of the fault every so often in the same direction and in the same magnitude on average. Note that in evaluating Figure 3-13 the considerations presented in Figures 3-6a and 3-6b should be kept in mind.

Figure 3-14 shows the consistency between the relative displacement rate vector and the geologically estimated slip rate vector associated with a thrust fault. Note again that in evaluating Figure 3-14 the considerations presented in Figures 3-7a and 3-7b should be kept in mind.

Figure 3-15a shows that the geologically estimated slip rate associated with the postulated thrust fault is comparable to the relative displacement rates (with respect to point A) associated with multiple GPS stations (B through F) located behind the hanging

wall side of the fault. In this case one should feel comfortable in saying that the postulated fault and its slip rate are consistent with the GPS data. However, if one selectively ignores the GPS stations B, C, D, and F without a good reason or if one has only one GPS station (E) behind the fault, then the resulting comparison or slip rate assignment based on the relative displacement rate from that GPS station can be misleading as indicated on Figure 3-15b. Thus, whenever possible, patterns of relative displacement rates from multiple GPS stations, rather than a single data point from a single station, should be used in evaluations.

3.1.7 Incremental Relative Displacement Rates

Figure 3-16a shows the GPS station A on one side and the GPS stations B, C, and D on the other side with two postulated faults in between: a strike slip fault with a high geologically estimated slip rate and a thrust fault with a low geologically estimated slip rate. Because the slip rate associated with the strike slip fault is so large relative to the slip rate associated with the thrust fault (the strike slip fault is dominating), the effect of the slip rate associated with the thrust fault may be difficult to discern when comparing the slip rates with the relative displacement rates.

Under these conditions, it may be useful to evaluate the "incremental" relative displacement rates, defined to be the relative displacement rate vector minus the geologically estimated slip rate vector associated with the a dominant fault. Such comparison of the geologically estimated slip rate associated with non-dominant fault with the incremental relative displacement rates is schematically illustrated on Figure 3-16b. The example shown on Figure 3-16b indicates that the relative displacement rate vectors at B, C, and D are not necessarily consistent with the slip rate vector associated with the postulated thrust fault. The result shown on Figure 3-16 could call to question the existence of the postulated thrust fault.

It is noted that incremental relative displacement rates should reflect the uncertainties not only of the error ellipse discussed in Section 3.1.4, but also the uncertainties associated with the slip rates of the dominant fault. Such uncertainties are not shown on Figure 3-16 for simplicity.

3.1.8 Summary Plots

Comparison of two parameters, slip rates and relative displacement rates, shown on Figures 3-13 through 3-16 is visual but somewhat awkward when one wants to compare simultaneously the magnitude and direction of these two parameters for a number of sites. For this reason, the detailed evaluations of the GPS data in this study use a "summary plot," developed as shown on Figure 3-17. The summary plot compares the combined slip rate vector with the relative displacement rate vector by:

- Putting their tails together at the origin,
- Indicating the uncertainties associated with their tips,

- Eliminating the line connecting the vector tail to the tip for the slip rate vector, and
- Indicating a thin straight-line segment connecting the tail to the tip for the relative displacement rate vector for visual differentiation.

For the slip rate vector on Figure 3-17a, a zone of dots shown on Figure 3-17b at the vector tip shows uncertainties associated with its tip. Each dot in this zone represents a specific combination of branches of the logic trees used to model the strike-slip fault intersected by a straight-line segment between the two GPS stations (point A and point B on Figure 3-17a) used in the calculation of the relative displacement rate. Although in the case of Figure 3-17a the straight-line segment connecting point A to point B intersects only a single strike-slip fault, in general, such a straight-line segment could intersect more than one fault. In such cases, each slip rate vector contributing to the uncertainty of the slip rate vector tip in the summary plot represents a vector sum of some specific series of slip rate vectors. Each of these slip rate vectors is associated with one of the faults intersected by the straight-line segment, out of all the combinations of the logic trees associated with all the faults.

For the relative displacement rate, uncertainties are the reported error ellipse of the relative displacement rate discussed in Section 3.1.4 increased by the uncertainties associated with the slip rate of the dominant seismic source (Section 3.1.7) when incremental relative displacement rates are involved.

Thus, a summary plot will show two uncertainty zones, one associated with the slip rates and the other associated with the relative displacement rate or incremental relative displacement rate. A thin straight-line segment connects the origin to the mean tip location of the relative displacement rate vector.

Assuming that the selected relative displacement rate between point A and point B on Figure 3-17 adequately reflects the release of tectonic ground straining associated with the fault that lies between the two points and assuming that all the strain release would not necessarily be seismogenic, the following criteria can be made:

- If the two uncertainty zones generally lie along the same line with the slip rate zone representing somewhat lower vector magnitude than the relative displacement rate zone, then the postulated fault(s) and the relative displacement rate can be considered consistent.

- As the two uncertainty zones deviate more from the above consistent conditions, the postulated fault(s) would become less consistent with the relative displacement rate from the GPS data.

3.2 OVERALL PATTERNS OF RELATIVE DISPLACEMENT RATES

Figure 3-18 shows the relative displacement rate vectors of the general set of SCIGN GPS stations listed on Figure 3-2 with respect to CAT1 located on Catalina Island, including the "reported" error ellipses. The star on Figure 3-18 indicates the approximate location of the SONGS site. As discussed earlier, these SCIGN GPS stations include all the SCIGN GPS stations in the general region of the SONGS site. Two observations can be made on Figure 3-18: none of the relative displacement rates appear to have any component in the expected slip rate direction of the postulated OBT, and CAT2 seems to be moving away from CAT1 toward the SONGS site.

Figure 3-19a shows the relative displacement rate vectors of the SCEC version 2 stations in the general region of the SONGS site with respect to CAT1. The observations made for Figure 3-18 in general appear to be applicable for this case also. Note that none of the relative displacement rate vectors "behind" the OBT have any compression component perpendicular to the strike of the OBT.

It can be noted on Figure 3-19a that there are three relative displacement rate vectors that do have small components consistent with OBT. One is at the SONGS site, another is somewhat northwest of the SONGS site, and the other is somewhat north of the SONGS site. However, there are only three of them, and two of them are along the coastal line rather than "behind" the OBT, indicating that it is unlikely that they alone would represent an adequate loading or driving mechanism for the postulated OBT. Furthermore, when one adds error ellipses on these relative displacement rates as shown on Figure 3-19b, the uncertainties associated with these three points are very significant.

Figure 3-20a shows the relative displacement rate vectors similar to those shown on Figure 3-19a except that they are with respect to the SONGS station. Figure 3-20a also clearly shows that none of the relative displacement rate vectors "behind" the OBT have any component consistent with the postulated OBT. Note also on Figure 3-20a that there appears to be some components of movement toward the SONGS site between Catalina Island and the SONGS site. However, in addition to the considerations provided with Figures 3-19a and 3-19b, the error ellipses associated with these and, in this case, just about all the rest of relative displacement rate vectors are very large as can be seen on Figure 3-20b.

3.3 TOTAL RELATIVE DISPLACEMENT RATES AND SLIP RATES

Figure 3-21 shows the selected SCIGN GPS stations with the geometry of Model 1 seismic sources. On Figure 3-21 the relative displacement rate vector of the SCIGN GPS station TRAK is shown with respect to the SCIGN GPS station CAT1. The straight-line segment connecting CAT1 with TRAK crosses the Palos Verdes fault, the Newport-Inglewood fault, and the San Joaquin Hills blind fault. Thus, the slip rate vector associated with the CAT1-TRAK pair to be used in the summary plot would reflect the vector sum of all the logic-tree combinations of the slip rate vectors from all of these seismic sources.

Figure 3-22a shows the summary plot associated with the CAT1-TRAK pair. The resulting slip rate vector tips are shown as dots on Figure 3-22a with the mean tip location shown by a darker and larger dot. The relative displacement rate vector is also shown on Figure 3-22a with the associated reported error ellipse. The relative displacement rate vector shown on Figure 3-22a can be referred to as the "total" relative displacement rate vector as opposed to "incremental" relative displacement rate vectors discussed in Section 3.1.7.

Many of the slip rate vector tips, shown as dots on Figure 3-22a, represent multiple data points. Therefore, the dots shown on Figure 3-22a have the third dimension corresponding to the number of data points within a given grid of two horizontal components. This fact is illustrated by a three-dimensional histogram shown on Figure 3-22b that corresponds to the dots shown on Figure 3-22a. The third dimension on Figure 3-22b is the fractional contribution of each grid combination. In the following sections, only two-dimensional distributions of the slip rate vector tips similar to that shown on Figure 3-22a are shown for convenience; however, it should be kept in mind that the actual distribution of dots is three-dimensional similar to that shown on Figure 3-22b.

Figures 3-23, 3-24, and 3-25 show the summary plots associated with Model 1, Model 2, and Model 3, respectively, each showing the summary plots corresponding to the 4 pairs of SCIGN GPS stations presented on Figure 3-12. On Figures 3-23 through 3-25, the total relative displacement rate vectors are shown. The summary plots of the 4 pairs are shown on each figure to emphasize the importance of evaluating the overall patterns of matching between the slip rates and the relative displacement rates, rather than focusing on any particular single pair.

On the basis of the criteria set at the end of Section 3.1.8, Model 1 appears quite consistent with the GPS data, followed by Model 2, then Model 3. In fact, Figure 3-23 indicates that Model 1 by itself adequately matches the GPS relative displacement rates corresponding to the 4 pairs. The introduction of Model 2 and Model 3 does not in any way contribute to an improvement in consistency, but rather, makes it less consistent for some stations.

3.4 INCREMENTAL RELATIVE DISPLACEMENT RATES

The slip rates shown on Figures 3-23 through 3-25 include the effects of the Palos Verdes fault, which has a slip rate ranging from 2 to 4 mm/year. Thus, the slip rates of the Palos Verdes fault dominate the "combined" slip rates shown on Figures 3-23 through 3-25. Under these conditions, it may be useful to evaluate the incremental relative displacement rates addressed in Section 3.1.7.

Figures 3-26, 3-27, and 3-28 show summary plots of the same 4 pairs of SCIGN GPS stations for Model 1, Model 2, and Model 3, respectively, but in terms of incremental relative displacement rates. Note that on Figures 3-26 through 3-28, the error ellipses for the relative displacement rate vectors have been increased to reflect the uncertainties

associated with the slip rate of the Palos Verdes fault in an approximate way. A comparison of Figures 3-26 through 3-28 with Figures 3-23 through 3-25 indicates that the observations made for Figures 3-23 through 3-25 also apply in general to the incremental relative displacement rates shown on Figures 3-26 through 3-28. Thus, eliminating the effects of the dominant Palos Verdes fault as modeled in this study does not change the strong consistency of Model 1 with the GPS relative displacement rates as well as the inconsistency of Model 2 and Model 3 with the GPS relative displacement rates.

3.5 SUMMARY

On the basis of a systematic evaluation of GPS data performed in this study, the following observations can be made:

- The overall patterns of relative displacement rates indicate that no compressional relative displacement fields exist behind the hanging wall side of the OBT postulated as part of Model 2 and Model 3.

- Both the total and incremental relative displacement rates associated with the 4 selected pairs of SCIGN GPS stations are adequately consistent with the slip rates associated with Model 1 fault sources.

- Both the total and incremental relative displacement rates associated with the 4 selected pairs of SCIGN GPS stations appear to become significantly inconsistent with the slip rates associated with the postulated Model 2 and Model 3 fault sources, with Model 3 being slightly less consistent than Model 2. Although for some pairs the consistency may improve for Model 2 and Model 3, it is the overall pattern of consistency that dictates the reasonableness of the postulated seismic sources.

- There may be some compressive strain occurring between some coastal areas near the SONGS site and Catalina Island. However, the reported error ellipses associated with these sites are large enough that the compressive component may well be within the uncertainties, and, in any case, the small compressive strain that may be occurring between the coastal area and Catalina Island is considered inadequate to load or drive the postulated OBT.

- A systematic evaluation of the available GPS data indicates that assigning weights to Model 2 and Model 3 higher than those presented in Section 2.0 is not justified. On the contrary, based strictly on the GPS data, one can make a good case for assigning weights significantly lower than those presented in Section 2.0 for Model 2 and Model 3.

- Finally, it is noted that where the patterns of GPS relative displacement rates indicate significant unaccounted compressional components in the direction perpendicular to the major strike-slip faults in the region, a conclusion

is often reached that thrust faults would likely accommodate the contraction (e.g., Bawden et al., 2001). In the region of the SONGS site, the absence of such patterns of significant GPS relative displacement rates in the direction perpendicular to the major strike-slip faults in the region, as shown in this section, makes it difficult to postulate significant active thrust faults in the region.

4.0 PROBABILISTIC SEISMIC HAZARD ANALYSIS

A probabilistic seismic hazard analysis (PSHA) was performed to evaluate the spectral acceleration values for the SONGS site using the seismic sources presented in Section 2.0. The probabilistic results of the SONGS IPEEE work are used as the previous results, and the 2001 PSHA results for Model 1 are used as the basis to discuss the effects of OBT as reflected in Models 2 and 3 (Section 2.0) as well as the effects of near-fault directivity and fling step (see Section 4.1.2 and 4.1.3, respectively) as a sensitivity study. In the sections to follow, the methodology used in the PSHA and the results of the PSHA are provided.

4.1 METHODOLOGY

In the following Sections 4.1.1, 4.1.2, and 4.1.3, the methodology used to perform the PSHA, the methodology used to incorporate the near-fault directivity effects into the PSHA results, and the methodology used to reflect the fling step effects in the PSHA results are, respectively, presented.

4.1.1 PSHA Methodology

General PSHA Methodology

The basic end result of PSHA, schematically shown as Step 5 on Figure 4-1, is a relationship between a ground motion parameter Z (peak ground acceleration and spectral acceleration in this study) and the mean number of events per year in which Z at the site exceeds a specified value z. This relationship is often termed a "hazard curve." The mean number of events per year is referred as "annual frequency of exceedance" and designated as "$\nu(Z \geq z)$". The inverse of this number is called the "average return period" (ARP) and is expressed in years. Once these relationships between appropriate parameters and annual frequency of exceedance are obtained, various probabilistic calculations can be made based on an assumption that the processes are Poissonian (Cornell, 1968).

In PSHA, a mathematical process is used to calculate the mean number of events per year in which the level of a ground parameter Z at the site exceeds a specified value z. Figure 4-1 schematically shows the five major components or steps in PSHA, which are based on Cornell (1968) and Kulkarni et al. (1979):

1. Characterization of seismogenic sources

   The location, geometry, and characteristics of seismic sources or earthquake faults relative to the site are evaluated and specified. The main characteristics of an earthquake fault consist of the segmentation model and segments, style of faulting, slip rate, dip, seismogenic depth, maximum or characteristic earthquake magnitude, and recurrence model. As shown in step 1 of Figure 4-1, an earthquake fault close to the site is

usually modeled as a three-dimensional planar source to reflect details of its geometry in the results. On the other hand, an earthquake fault far from the site is usually modeled as a linear (piecewise linear) source because details of its geometry with respect to the site have negligible effects on the results. However, in this study all the faults were modeled in a three-dimensional manner.

2. Specification of recurrence relationship

Apart from the geometry, the most important characteristic of a fault is its recurrence relationship or the relationship showing the annual recurrence of earthquakes of various magnitudes, up to the maximum magnitude, on each fault. This relationship is schematically shown in step 2 of Figure 4-1 in its usual cumulative form: earthquake magnitude m versus mean number of earthquakes per year having magnitude greater than m on a fault. As schematically shown on step 2 of Figure 4-1, this relationship is used to provide the mean number of earthquakes $\dot{N}_s(m_j)$ having a particular magnitude m_j on a given fault during a 1-year period. This is accomplished by evaluating an increment around magnitude m_j.

3. Evaluation of probability of distance to rupture

Given an earthquake magnitude m_j on a particular fault, a typical rupture plane associated with m_j is postulated as schematically indicated in step 3 of Figure 4-1. Using an assumption that the typical rupture plane can occur anywhere along the plane of the seismic source with an equal probability, the probability that the typical rupture plane is at a specified distance, r_k, from the site is calculated for the given m_j. This probability is assessed by considering the geometry of the fault, the relationship between the rupture area and magnitude, and the distance definition used in the particular attenuation relationship being considered.

4. Calculation of exceedance using the attenuation equation

The probability that the ground motion parameter Z from the earthquake of a certain magnitude (m_j) occurring at a certain distance (r_k) on a particular fault will exceed a specified level z at the site is calculated by integration, which is schematically shown in step 4 of Figure 4-1. This probability is based on the selected attenuation equation considering its standard error term and the site conditions.

5. Calculation of probabilistic seismic hazard

By combining the three probability functions associated with steps 2 through 4 of Figure 4-1 for each fault (summing over r_k for each m_j and then summing over m_j), the mean number of events per year (annual

frequency of exceedance or $\nu(Z \geq z)$) resulting in Z being greater than z at the site is computed for that fault. This process is repeated a sufficient number of times to cover all the faults, and the contributions are added to obtain the total seismic hazard at the site for a given z level. The complete hazard curve is obtained by repeating these computations for several levels of ground motion parameter Z. This process is schematically shown in step 5 of Figure 4-1.

Once this mean number of events per year $\nu(Z \geq z)$ is obtained, the probability of the level of the ground motion parameter being exceeded over a specified time period, t, can be calculated by the following equation based on the Poisson model:

$$Pr(Z \geq z) = 1 - \exp[-\nu(Z \geq z) \cdot t] \quad \textbf{(4-1)}$$

Attenuation Relationships

Attenuation relationships used in the SONGS IPEEE study were Abrahamson (1994), Boore et al. (1994), Sadigh (1994), Campbell (1993), (Campbell and Bozorgnia, 1994) and Idriss (1987, 1994). Attenuation relationships used in the current PSHA were chosen to be similar to but more current than those used in the SONGS IPEEE study. However, the Idriss relationship, which has not been updated since the SONGS IPEEE study and had a lower weight of 0.15 in the SONGS IPEEE study, was dropped in this study.

The attenuation relationships selected in this study are as follows:

- Abrahamson and Silva (1997)
- Boore et al. (1997)
- Sadigh et al. (1997)
- Bozorgnia et al. (1999), which is an updated version of Campbell (1997)

For the Abrahamson and Silva, Sadigh et al., and Bozorgnia et al. relationships, the soils site relationships were used. In the Bozorgnia et al. relationship, a depth to basement rock of 3 km was used as in the SONGS IPEEE study. In the Boore et al. relationship, an average shear wave velocity of 1,450 feet/second in the upper 100 feet was used. The equal weight of ¼ was used for all the attenuation relationships, and the standard error terms as reported in individual relationships were used without any modifications. The ground motion distributions were truncated at plus and minus 3 standard errors.

Uncertainties

Two major types of uncertainties addressed in the PSHA used in this study are as follows:

- Aleatory Uncertainty. This uncertainty is a reflection of the "randomness" inherent to the natural phenomenon of earthquake generation and ground

motions. This uncertainty may in part be based on the limited scientific understanding of the natural phenomenon of earthquake generation and seismic wave propagation. However, even if we had a large amount of geologic and seismicity data on past seismic activity, the exact prediction of the time, location, and characteristics of future earthquakes is still not possible. Uncertainties in the earthquake recurrence process and in the attenuation of ground motion are the major sources of the aleatory uncertainty.

- Epistemic Uncertainty. This uncertainty is a reflection of the limited data available to estimate the parameters contributing to the seismic hazard at a site. This type of uncertainty, in theory, can be reduced when additional data or understanding of earthquakes and their effects become available.

The PSHA methodology includes probability models to address these two major types of uncertainty. Aleatory uncertainty is addressed in the PSHA model through probabilistic distributions (such as those associated with attenuation relationships as schematically indicated in step 4 of Figure 4-1).

The epistemic uncertainty in the various input parameters for key seismic sources is reflected in the PSHA by using a logic tree approach (Kulkarni et al., 1984; Coppersmith and Youngs, 1986; Reiter, 1990). Figures 2-18 and 2-19 show a portion of the logic tree used in this study.

The probability model described previously assumes that the parameters indicated on Figures 4-1 are known, or can be estimated precisely. In practice, only limited data are available to estimate these parameters. Consequently, the estimates of the parameters are subject to epistemic uncertainty. Using the logic tree approach, the epistemic uncertainty in the input parameters is propagated to obtain not only the best estimate of the annual frequency of exceeding a given level of ground motion, but also the confidence limits of this best estimate.

4.1.2 Directivity Effects Methodology

The rupture directivity effects at a given site are expected from earthquakes that have rupture faults near that site and affect ground motions in a frequency range lower than about 1 Hz. The available attenuation relationships do not explicitly include the near-fault directivity effects (Somerville et al., 1997). However, response spectral values in a low frequency range can be adjusted to account for the near-fault directivity effects using the approach proposed by Somerville, et al. (1997). In this approach the published attenuation relationships for horizontal ground motions are modified through two frequency-dependent scaling factors to account for the following:

(1) Change in shaking level in the average (FA) horizontal component of ground shaking due to near-fault rupture directivity effects (higher ground shaking for rupture toward the site, and lower ground shaking for rupture away from the site), and

(2) Changes in two ratios: the ratio of fault normal (FN) ground shaking to the FA horizontal ground shaking and the ratio of fault parallel (FP) ground shaking to FA horizontal ground shaking.

Modifications to the Somerville approach were made by Abrahamson (2000) to reflect reasonable saturation effects of rupture distance and to make this approach directly applicable to PSHA. Among these modifications, Abrahamson introduced the following two taper functions:

- One that reduces the directivity scaling factor to zero for distances greater than 60 km, and

- One that constrains the directivity scaling factor to vary linearly between moment magnitudes of 6.0 to 6.5 (i.e., at magnitude less than 6.0, the scaling factor is zero, and for magnitude greater than 6.5, the scaling factor is maintained to be the same as that for magnitude 6.5).

For rupture directivity effects generated from strike-slip event, the Somerville approach uses two directivity parameters, x and θ (see Figure 4-2), where x is defined as the fraction of the fault length that ruptures toward the site and θ the angle between the fault strike and epicentral azimuth (see Figure 4-2). In the Somerville approach, no upper bound limit was imposed on these two parameters. However, Abrahamson (2000) suggested that there is little empirical data to support x cos(θ) values greater than 0.6, and the extrapolation of the model to larger x cos(θ) values is not well constrained. Based on an evaluation of empirical recordings and numerical simulations, Abrahamson recommended that the form of the directivity function be modified so that x reaches a maximum value of 0.4. Abrahamson did not suggest any modification to fault rupture directivity parameters y and ϕ (see Figure 4-2) for dip-slip events.

Abrahamson (2000) also noted that including the directivity effect should result in a reduction of the standard deviation of the attenuation relationship. Based on evaluation of empirical data, Abrahamson noted that at a period of 3 seconds (frequency of 0.33 Hz), the reduction of the standard deviation is about 0.05 natural log units. This reduction is caused by the addition of the directivity term into the ground motion model. Therefore, Abrahamson (2000) also provided modifications to the standard error of the attenuation relationship to take into consideration the addition of the directivity effect.

The final modified Somerville model for the fault normal horizontal component for strike-slip model is given by:

$$\ln Sa_{dir}(M,r,x,\theta,T) = \ln Sa(M,r) + y_{dir}(x,\theta,T)\cdot T_d(r)\cdot T_M(M) \qquad \textbf{(4-2)}$$

where,

$Sa_{dir}(M,r,x,\theta,T)$ = Average horizontal spectral component including directivity,

$Sa(M,r)$	=	Average horizontal spectral component without directivity,
$y_{dir}(x,\theta,T)$	=	Modified Somerville, et al (1997) relationship (provided in Abrahamson (2000) with errata correction to use: "x $\leq$ 0.4" or "x > 0.4" rather than "x cos(θ) $\leq$ 0.4" or "x cos(θ) > 0.4", respectively),
$T_d(r)$	=	Taper function to limit the directivity effect for distance less than 60 km,
$T_m(M)$	=	Taper function to allow the full directivity effect for magnitude higher than 6.5, but to reduce the directivity effect from full to zero linearly from magnitude 6.5 to magnitude 6,
r	=	Closest distance to fault rupture, km
M	=	Moment magnitude, and
T	=	Period, in seconds.

For the fault parallel component, "+" sign in equation (4-2) should be replaced by "-" sign.

As indicated above, for the dip-slip model, the Somerville (1997) approach was used without modifications for this case because Abrahamson provided no modification.

As suggested by Abrahamson (2000), the rupture directivity effect was directly incorporated in PSHA by introducing an additional step into the standard PSHA calculation to account for the location of the hypocenter on the rupture area. In the present study, it was assumed that the hypocenter of the rupture area is uniformly distributed throughout the rupture area (i.e., no preferred locations for the nucleation of the rupture).

4.1.3 Fling Step Effects Methodology

The fling is defined as the ground motion at the site caused by tectonic deformation that accompanies earthquake shaking. This effect should be reflected only in ground motions near causative faults. Based on observed displacement from the 1999 Koaceli (Turkey) earthquake, Abrahamson (personal communication, October 10, 2001) developed the functional form of the fling as shown on Figure 4-3. The functional form of the fling adopted by Abrahamson consists of an acceleration pulse of a sine wave that results in finite tectonic displacement (i.e., finite ground displacement after double integration of the acceleration time history). The functional form of the fling step is given by:

$$
\begin{aligned}
&Acc_{fling}(t) = 0 && \text{for } t<t_1 \\
&Acc_{fling}(t) = A\sin(\omega(t-t1) && \text{for } t_1<t<t_1+T_{fling} \\
&Acc_{fling}(t)=0 && \text{for } t_1+T_{fling}<t
\end{aligned}
\qquad \textbf{(4-3)}
$$

where, $\omega=2\pi/T_{fling}$.

Strike-Slip Fling Parameters

Abrahamson obtained amplitude (A) and period (T_{fling}) of the fling pulse for strike-slip events by evaluating recorded data and considerations about the average slip on the fault. Based on the Abrahamson approach, displacement at the fault, D_{fault}, which is used for magnitude scaling purposes, is provided by the following equation:

$$\ln(D_{fault}) = 1.15M - 2.83 \qquad \textbf{(4-4)}$$

where, M is the seismic moment magnitude and D_{fault} is in cm.

Based on observed tectonic deformations from large strike-slip earthquakes, Abrahamson developed a relationship for evaluation of displacement at a site located away from the fault, D_{site}, as follows:

$$D_{site} = 0.5 \cdot D_{fault} \cdot \cot^{-1}(\alpha \cdot r)/(\pi/2) \qquad \textbf{(4-5)}$$

where, r, is the closest distance to the rupture area, and α is a model constant obtained from empirical data based on observed records. For a strike-slip fault, regression of the observed record yielded 0.22 for the value of α.

Double integrating the fling functional form and equating the resulting displacement to that obtained from equation (4-5) above yields the amplitude of the fling step acceleration time history as:

$$A(g) = \frac{D_{site} \cdot 2\pi}{981 \cdot T_{fling}^2} \qquad \textbf{(4-6)}$$

Based on recorded data, Abrahamson (personal communication, October 10, 2001) computed a standard deviation of ln(A), $\sigma_{ln(A)}$, as 0.95.

The period of the fling step, also obtained by Abrahamson through evaluation of recorded data for both strike-slip and dip-slip earthquakes, is provided as follows:

$$\ln(T_{fling}\,(\text{in sec})) = -6.96 + 1.15\,M \qquad \textbf{(4-7)}$$

The standard deviation of the $\ln(T_{fling})$, $\sigma_{\ln(Tfling)}$, is 0.34. The value of the fling period can then be substituted into equation (4-6) to obtain the amplitude of the fling step. The actual amplitude and period of the fling step used in the present study correspond to 84th

percentile values. Use of the 84th percentile fling for the Safe Shutdown Earthquake (SSE) is consistent with the SSE being an 84th percentile ground motion.

Dip-Slip Fling Parameters

The model for the D_{site} parameter is given in equation (4-5) for the strike-slip style of faulting. For a dip-slip event, such as the OBT, D_{site} needs to be re-evaluated. The tectonic deformation on the hanging wall and foot sides of the fault will not be symmetrical. Because of limited tectonic data available for dip-slip style of faulting (Abrahamson, personal communication, October 10, 2001), we have selected the tectonic deformation data measured from the 1994 Northridge earthquake (Hudnut, et al., 1996) for use in the present study to evaluate the tectonic displacement for this style of faulting.

Displacement for a location directly adjacent to the fault was computed using equation (4-5). The distribution of D_{site} from the Northridge event is shown on Figure 4-4. Based on this data, an upper bound relationship for D_{site} was selected as:

$$D_{site,UpperBound} = 0.5 \cdot D_{fault} \cdot \cot^{-1}(0.24 \cdot r)/(\pi/2) \qquad \textbf{(4-8)}$$

This value of D_{site} was used to evaluate the amplitude of dip-slip event. Period of the dip-slip fling step is computed using equation (4-7).

Design Response Spectra Including Fling Step

The fling step effect can be incorporated into ground motions only in the time domain (i.e., through adjustments to acceleration time histories). Therefore, a recorded time history must be selected first and matched to the design response spectra to provide the design time history. The fling step time history is then added to the design time history to provide the final design time history including fling step effect. The fling is assumed to arrive at the time of the beginning of the large velocity pulse corresponding to the S waves (Abrahamson, personal communication, October 10, 2001), based on empirical observations and numerical modeling results. The basis for this assumption is that it is conservative because it maximizes the constructive interference between the fling ground motion due to permanent displacement and the shaking due to transient displacement. The response spectrum of the resulting time history is computed to provide the design response spectra including the fling step effect.

It is noted that for an earthquake event on a strike-slip fault, the fling affects only the component of the ground motion parallel to the strike of the fault, whereas for a dip-slip event, the fling affects the component of the ground motion perpendicular to the fault (i.e., the fault normal component).

In this study, these fling effects were evaluated for the maximum magnitude, and the resulting effects on response spectra were enveloped. This very conservative approach was adopted in this study because of the following considerations:

- A probabilistic method to incorporate the fling step effects is not currently available.
- Reflecting the fling step effects in a realistic way would be rather complicated because of the two different types of near-by seismic sources affecting the ground motions at the SONGS site (OZD and OBT).
- The effects on the resulting response spectra are not significant.

4.1.4 Weighted Hazard Curve

To be consistent with the seismic hazard curve from the SONGS IPEEE work, it was desirable to develop the seismic hazard curve with spectral ground accelerations averaged over the frequencies from 1 to 10 Hz in this study. The frequency range of 1 to 10 Hz was considered to reflect the frequencies of structures and components that dominate the seismic risk at SONGS.

The weighted hazard curve is a relationship between the weighted spectral acceleration values and annual probability of exceedance, which goes down to 1×10^{-8}. The annual probability of exceedance is evaluated through PSHA following the methodology presented in Section 4.1.1. At each annual probability of exceedance level, the weighted spectral values are obtained as shown on Figure 4-5. Spectral accelerations at frequencies of 1 Hz and 10 Hz are each multiplied by ½ and then added to the sum of spectral accelerations at frequencies of 5 Hz and 2.5 Hz, and the resulting sum is divided by 3.

4.2 SONGS IPEEE RESULTS

Figure 4-6 shows the mean hazard curves at 25 Hz and 5 Hz from the SONGS IPEEE study. Figure 4-7 shows the mean uniform hazard response spectra at the Safe Shutdown Earthquake (SSE) level from the SONGS IPEEE study. Finally, Figure 4-8 shows the mean weighted hazard curve from the SONGS IPEEE study down to an annual probability of exceedance of 10^{-8}. These probabilistic ground motion results from the SONGS IPEEE study are listed in Table 4-1. These results are collectively or individually referred to as the "previous" results herein.

4.3 NEW PROBABILISTIC RESULTS

The results of the current (2001) PSHA using Model 1, Model 2, and Model 3 discussed in Section 2.0 are presented in the following sections. All the PSHA results presented are mean results.

4.3.1 Base Results

As discussed earlier, Model 1 used in the 2001 PSHA is the 2001 version of the seismic source model used in the SONGS IPEEE work because it is very similar to the IPEEE seismic source model except for the inclusion of SJBF in Model 1. Thus, the 2001 PSHA results using only Model 1 are referred to as the "base" results herein.

Figure 4-9 compares the previous hazard curves at 5 Hz and 25 Hz with the hazard curves at the same frequencies obtained for Model 1 from the current 2001 PSHA. As can be seen from Figure 4-9, at 25 Hz the previous hazard curve is only very slightly lower than the 2001 base hazard curve, but at 5 Hz the previous hazard curve is significantly higher than the base hazard curve.

Figure 4-10 compares the previous uniform hazard response spectrum at the SSE level with the uniform hazard response spectrum at the same level for Model 1 from the 2001 PSHA results. The SSE Model 1 uniform hazard spectrum shown on Figure 4-10 correspond to the annual probability of 1.74×10^{-4}. The probability level is based on the points on the combined (see Section 4.3.2) peak acceleration hazard curve associated with 0.67 g. As can be seen on Figure 4-10, the 2001 response spectra are shifted toward a low frequency range compared to the previous response spectra. In addition, the IPEEE response spectra are significantly higher than the previous results at a frequency of 5 Hz. In addition to the use of a newer version of each attenuation relationship, these general changes basically were caused by the following changes in attenuation relationships from the SONGS IPEEE PSHA to the 2001 PSHA:

- Elimination of the attenuation relationship by Idriss (1987, 1994), which was for sites stiffer than the SONGS site (note that this relationship had the lowest weight in the SONGS IPEEE PSHA)
- Specification of the attenuation relationship by Boore et al. (1997) based on an average shear wave velocity of 1,450 feet/seconds in the upper 100 feet from that of the attenuation relationship by Boore et al. (1994) based on an average of site conditions B and C.

Both of the above changes tend to shift the response spectra toward a lower frequency range consistent with the trend shown on Figure 4-10 and the trend expected for the SONGS site based on the 1,450 feet/second average shear wave velocity in the upper 100 feet.

Therefore, from the site stiffness point of view, the current set of attenuation relationships and, thus, the shifted response spectra shown on Figure 4-10 are considered more current for the SONGS site than the previous relationships used in the SONGS IPEEE study.

Figure 4-11 compares the previous weighted hazard curves with the weighted hazard curve for Model 1 from the current PSHA results. Figure 4-11 shows that the Model 1 results become somewhat lower than the previous results, particularly at low annual probability of exceedance levels, and become somewhat higher only at annual probability of exceedance levels higher than about 3×10^{-3}.

4.3.2 Effects of OBT

In this section the effects of OBT are addressed by comparing the 2001 PSHA results for Model 1 with the "combined OBT results," which reflect the weighted average of Model 1, Model 2, and Model 3 per Section 2.0 (weights of 0.70, 0.25, and 0.05, respectively), where

Models 2 and 3 reflect the presence of OBT. Thus, the Model 1 or base case is compared to the OBT case as reflected in the combined PSHA results. It should be noted that in this section all the PSHA results presented do not reflect the directivity or fling step effects.

Figure 4-12 compares the hazard curves at 5 Hz and 25 Hz for Model 1 with the hazard curves at the same frequencies for the combined OBT results all from the 2001 PSHA results. As can be seen on Figure 4-12, the combined OBT results are higher than the base case corresponding to Model 1.

Figure 4-13 compares the uniform hazard response spectrum at the SSE level for Model 1 with the uniform hazard response spectrum at the same hazard level for the combined OBT results, all from the 2001 PSHA results. The annual probability associated with uniform hazard spectrum shown on Figure 4-13 for the SSE is 1.74×10^{-4}. As can be seen on Figure 4-13, the combined OBT response spectrum is higher when compared to the base case of Model 1.

Figure 4-14 compares the weighted hazard curve for Model 1 with the weighted hazard curve for the combined OBT results, all from the 2001 PSHA results. Figure 4-14 indicates that the weighted hazard curve associated with the combined OBT is higher, particularly at very low values of annual probability of exceedance.

4.3.3 Effects of Directivity

In this section the effects of near-fault directivity are addressed by comparing the 2001 PSHA results for the combined OBT without the directivity effects with the results from the combined OBT with the directivity effects. It should be noted that in this section all the PSHA results presented do not reflect the fling step effects.

Figure 4-15 compares the hazard curves at 0.5 Hz and 1 Hz for the combined OBT results without directivity or fling step effects with the hazard curves at the same frequencies for the combined OBT results with the directivity effects (but no fling step effects), all from the 2001 PSHA results. On Figure 4-15 the hazard curves are compared at frequencies of 0.5 and 1 Hz because the effects of directivity will not show up in the hazard curves at frequencies of 5 or 25 Hz. As expected, the directivity effects are higher at a frequency of 0.5 Hz rather than at 1 Hz.

Figure 4-16 compares the uniform hazard response spectrum at the SSE level for the combined OBT results without directivity or fling step effects with the uniform hazard response spectrum for the combined OBT results with the directivity effects (but no fling step effects), all from the 2001 PSHA results. Again, the effects of directivity are small.

Figure 4-17 compares the weighted hazard curve for the combined OBT results without directivity or fling step effects with the weighted hazard curve for the combined OBT results with the directivity effects (but no fling step effects), all from the 2001 PSHA results. Because the weighted hazard does not include frequencies less than 1 Hz (Figure 4-5), the effects of directivity on the weighted hazard curve are essentially negligible.

4.3.4 Effects of the Fling Step

Figure 4-18 shows the effects of the fling step on the uniform hazard response spectrum at the SSE level for the combined OBT results reflecting the directivity effects, all from the 2001 PSHA results. The effects of the fling step increase response spectral values by less than 2 percent at 0.5 Hz and about 1 percent at 1 Hz. The fling step does not affect response spectral values at frequencies higher than about 1 Hz. The fling step effects reflected on Figure 4-18 were based on the Lucerne record (the 1992 Landers earthquake) with A of 0.057g, T_{fling} of 2.6 sec, and M_w of 6.8 for the OZD and the Newhall record (the 1994 Northridge earthquake) with A of 0.012g, T_{fling} of 6.5 sec, and Mw of 7.8 for the OBT. Except for Mw, these values of the fling step parameters were computed using the methodology described in Section 4.1.3.

4.4 SUMMARY

Using the seismic sources discussed in Section 2.0 and the PSHA methodology discussed in Sections 4.1.1 through 4.1.4, PSHA was performed to evaluate the effects of the postulated OBT. The effects of OBT were evaluated by comparing the new PSHA results using Model 1, which does not include OBT, with the PSHA results that combined the Model 1, Model 2, and Model 3, which reflect the effects of OBT through appropriate weighting (0.70, 0.25, and 0.05, respectively, for Model 1, Model 2, and Model 3) on each model as discussed in Section 2.0.

On the basis of these evaluations, the following observations can be made:

- In general, the hazard curves, response spectra, and weighted hazard curves for the combined OBT case are higher than those from Model 1 with the differences being greater at lower annual frequency of exceedance levels.
- The effects of directivity appear to be no more than about a 2 percent increase at 1 Hz and 8 percent increase at 0.5 Hz for the SSE level.
- Given the above observation and given that the evaluation of GPS data indicates that the weights assigned to Models 2 and 3 may be too high, the results of the 2001 PSHA for the combined OBT case should be conservative.
- The effects of the fling step appear to be even less at no more than about a 2 percent additional increase in spectral acceleration values at 0.5 Hz and about an 1 percent additional increase at 1 Hz.

In addition, this summary section compares the 2001 combined PSHA results reflecting the directivity and fling step effects with the previous results from the SONGS IPEEE study. Figure 4-19 shows the 2001 hazard curves at 5 Hz and 25 Hz for the combined OBT results reflecting the directivity and fling step effects. Figure 4-19 also shows the SONGS IPEEE hazard curves at the same frequencies for comparison. Although the 2001 results are higher at 25 Hz and lower at 5 Hz, they are not significantly different from the corresponding results from the SONGS IPEEE study.

Figure 4-20 shows the 2001 hazard curves at 5 Hz and 25 Hz shown on Figure 4-19 and indicates the relative contributions of the NI/OZD/RC/OBT sources and the rest of the sources. From Figure 4-20 it is clear that for an annual probability of exceedance lower than about $3x10^{-3}$, the NI/OZD/RC/OBT completely dominates the hazard. It should be noted, however, at an extremely low annual probability of exceedance (about 10^{-7} or less range), the floating seismic source starts to have significant effects on the seismic hazard at the SONGS site.

Figure 4-21 shows the 2001 uniform hazard response spectrum at the SSE level for the combined OBT results reflecting the directivity and fling step effects. Figure 4-21 also shows the SONGS IPEEE uniform hazard response spectrum at the same level for comparison. Figure 4-22 shows the 2001 weighted hazard curve for the combined results (Model 1, Model 2, and Model 3) reflecting the directivity and fling step effects. Figure 4-22 also shows the SONGS IPEEE weighted hazard curve for comparison. Overall the 2001 weighted hazard curve is comparable to the SONGS IPEEE weighted hazard curve.

The numerical results of the 2001 PSHA are listed in Table 4-2 in terms of those without directivity or fling step effects, with directivity effects only, and with both the directivity and fling step effects.

5.0 SEISMIC PROBABILISTIC RISK ANALYSIS

5.1 METHODOLOGY

In order to evaluate the effect of considering the postulated blind thrust faults on the seismic risk at SONGS, the seismic probabilistic risk analysis (PRA) was focused on the potential increase in core damage and large early release risk due to postulated blind thrusts. The SONGS Living PRA, which includes external events, was used to assess this potential increase. Since the submittal of the IPEEE (SCE letter to NRC dated December 15, 1995), the plant and the plant model have undergone a number of risk reducing plant modifications and model improvements, respectively. These improvements have been included in the SONGS Living PRA and are included in this study. The SONGS Living PRA reflects the as-built plant.

To calculate the risk impact of the postulated blind thrusts, the baseline risk is assessed using the current SONGS Living PRA. This is compared against the postulated risk as assessed by substituting the postulated seismic hazard curve in the current SONGS Living PRA. The risk difference, or risk increase, is evaluated for core damage frequency (CDF) and large, early release frequency (LERF).

The SONGS Living PRA model consists of the seismic hazard curve, seismic event tree, component fragilities, and the internal events PRA model. Except for the seismic hazard curve, all other model components remained constant in the calculation. The baseline seismic hazard curve for this calculation was developed for the SONGS IPEEE.

5.1.1 Seismic Fragilities

The 2001 Uniform Hazard Spectrum was compared to the SONGS IPEEE Uniform Hazard Spectrum to determine whether the seismic fragilities of the plant's structures and components needed to be revised. The Uniform Hazard Spectrum is used to define the free-field ground motion for calculating the structural responses.

As discussed in the SONGS IPEEE, in-structure response spectra were generated based on time-history analysis of soil-structure interaction models, using three-dimensional stick–model representations of buildings. The overall approach for assessing structural responses and component demands consisted of the following steps:

- Specify the free-field ground motion
- Develop soil models
- Compute free-field soil responses and determine strain-compatible soil properties
- Calculate foundation impedance functions and wave scattering effects
- Model the characteristics of the fixed base structure
- Perform the Soil-Structure Interaction (SSI) analysis for the coupled soil-structure system

- Conduct SSI analysis for a suite of input combinations to develop probabilistic responses.

Response calculations were performed for seismic excitation at the SSE level. The free-field ground motion (located at the soil surface, away from structures) was defined by the Uniform Hazard Spectrum (UHS) shape at the SSE level. These motions were scaled to a common value of the ground motion parameter Sa (1-10 Hz).

Variability in soil shear modulus, soil damping, structural frequency, and structural damping were assigned and used to develop simulations for these parameters. These model parameters were then combined with the 26 motion time histories to develop 26 different variations (of motion/SSI model parameters) for conducting SSI analyses. Results from the 26 response analyses were used to derive the structural responses and component demands, including the median demands.

Referring to Figure 4-21, at the SSE level the 2001 UHS is slightly higher than the SONGS IPEEE at frequencies below 1.5 Hz and is lower at frequencies above about 2 Hz. Since the lowest natural frequencies of SONGS structures are about 1.5 Hz and most components have natural frequencies above 4 Hz, there would be no decrease in the seismic fragilities that were calculated for the SONGS IPEEE. Also, based on the lower accelerations in the 2 Hz and above range, seismic demand on components would be less and thus could result in higher seismic fragility values. So, the seismic fragilities were not revised for the PRA model of this study.

5.1.2 Seismic Probabilistic Risk Analysis

The seismic hazard curve is input into the seismic PRA model to simulate the probabilities of failure of structures and components. As described in Section 4, the seismic hazard curve for the 2001 seismic source model is higher than the SONGS IPEEE seismic hazard curve (Figure 4-22). To determine the risk significance of the 2001 PSHA hazard curve, the core damage frequency (CDF) and large, early release frequency (LERF) associated with each curve is quantified.

Using the IPEEE hazard curve and the methodology employed in the seismic IPEEE, the potential combinations of seismic-induced and random failures that lead to core damage and large early release are quantified using the SONGS 2/3 Living PRA. This quantification reflects the risk associated with the IPEEE hazard curve. The risk impact of the 2001 PSHA hazard curve is calculated by replacing the IPEEE hazard curve with the postulated seismic hazard curve and requantifying the SONGS 2/3 Living PRA. The risk significance of the 2001 PSHA hazard curve is the calculated difference in risk (CDF and LERF) associated with each curve.

5.2 PRA RESULTS

From the SONGS 2/3 Living PRA, the current average SONGS CDF and LERF from internal and external events are 4.27E-5/year and 1.60E-6/year, respectively. Substituting the seismic hazard curve to include the postulated blind thrusts results in a total average core damage and large, early release risk of 4.57E-5/year and 1.78E-6/year. These are postulated increases of 3.0E-6/year and 1.8E-7/year.

There were no plant vulnerabilities identified in the PRA when the seismic hazard curve includes considerations for the postulated blind thrusts.

5.3 SUMMARY

While the Uniform Hazard Spectrum exhibits some small increases in spectral accelerations at lower frequencies of less than 1.5 Hz, there would be negligible effect on the structural responses of the SONGS IPEEE buildings because the structures have natural frequencies of about 1.5 Hz and higher. The decrease in spectral accelerations at the higher frequencies above 1.5 Hz would have the effect of reducing the seismic demands on components. Therefore, the SONGS IPEEE seismic fragilities were not revised for input into the PRA model.

Following the methodology used in the SONGS 2/3 Seismic IPEEE, the risk associated with the seismic IPEEE hazard curve (current hazard curve) and 2001 PSHA hazard curve is quantified. From the SONGS 2/3 Living PRA, the current average SONGS CDF and LERF from internal and external events are 4.27E-5/year and 1.60E-6/year, respectively. Substituting the seismic hazard curve to include the postulated blind thrusts results in a total average core damage and large, early release risk or 4.57E-5/year and 1.78E-6/year. These are postulated increases in CDF and LERF of 3.0E-6/year and 1.8E-7/year, respectively.

The seismic PRA results show that there would be no vulnerabilities at SONGS and the increase in core damage frequency is small. Therefore, the postulated blind thrusts would not appreciably change the seismic risk of SONGS.

6.0 CONCLUSIONS

Seismic Source Characterization

The seismic source characterization model developed for this study updates the source model previously developed as part of the seismic risk analysis for the SONGS Individual Plant Examination of External Events (IPEEE) (SCE letter dated December 15, 1995; Risk Engineering, 1995. Appendix A). In particular this study evaluated recently postulated blind thrust faults in the vicinity of SONGS (i.e., the Oceanside blind thrust (OBT) and San Joaquin Hills blind fault (SJBF)) that were not explicitly modeled in the IPEEE study. For this study, three alternative source characterization models were developed to capture the range of plausible fault source geometries and interactions between the postulated thrust and strike-slip faults that could have a significant impact on the seismic hazard to SONGS.

Model 1-Strike Slip Model -This model assumes that there is a through-going strike slip fault system (the NI-SCOZD-RC) that extends to seismogenic depth. In this model the Oceanside detachment is not considered to be an active seismogenic source. A blind thrust fault underlying the San Joaquin Hills (the SJBF) is included as a potential seismogenic fault source with a probability of activity (i.e., it behaves as an independent seismic source) of 0.5.

Model 2-Independent OBT and Strike-slip faults - In this model, the Oceanside blind thrust (OBT) is considered to be an active seismogenic source. Two alternatives are considered, depending on whether or not the San Joaquin Hills blind fault (SJBF) is linked (i.e., is a backthrust) to the OBT. The NI and RC are modeled as independent strike-slip faults.

Model 3-OBT Oblique - In this model, the OBT and SCOZD-RC represent strain partitioning in the upper crust (thrust and strike-slip, respectively) above a single oblique-slip fault plane (OBT-oblique) at depth. The NI is modeled as an independent strike-slip fault.

Based on consideration of the evidence for the activity and seismogenic potential of these faults, as well as geologic and geodetic evidence that pertain to the style and rate of deformation that is occurring in the present tectonic environment, weights were assigned to the models as follows: Model 1 (0.7); Model 2 (0.25); and Model 3 (0.05). Although there is general agreement in the professional and academic communities that detachment faults are present in the inner California borderland, there is no direct evidence that clearly demonstrates that these faults have been reactivated as blind thrust faults on a regional scale. Evidence presented by Rivero and others (2000) regarding the level of activity, slip rate, and seismogenic potential of the OBT as a source of future large magnitude earthquakes is inconclusive. Uncertainties in the interaction of the postulated OBT and recognized strike slip faults (NI and RC) are accounted for by Models 2 and 3. Model 2 is judged to be a more viable structural model and therefore is given higher weight.

A much stronger case is made in support of the model that characterizes the South Coast Offshore Zone of Deformation (SCOZD) as part of a through-going strike-slip fault zone. The chief arguments supporting the higher weight given to the strike-slip model (Model 1) are:

- Interpretations of 2D and high-resolution shallow seismic data show evidence for a relatively continuous zone of recent deformation linking the Rose Canyon (RC) and Newport-Inglewood (NI). Seismicity and paleoseismic data show that the NI and RC faults are capable strike-slip faults

- Geodetic data show that strain in the southern Californian inner borderland is characterized by north-northwest directed shear subparallel to the overall North America/Pacific plate motion. Little or no convergence across the inner borderland in the vicinity of SONGS is indicated in the geodetic data. In particular, the lack of significant convergence in the regional signal to the east of the OBT suggests there is not a regional "driving" force that would reactivate a large seismogenic thrust.

- Fault and fold deformation observed along the SCOZD is consistent with transpressional right lateral slip along a N20°W trending fault. Evidence to support reactivation of the entire OBT in the current tectonic environment is not demonstrated. Seismicity and possible late Pleistocene/Holocene faults and associated folding can be explained by localized reactivation (strain partitioning) and contraction in left steps or bends in a transpressional right-slip tectonic environment. Clockwise rotation of crustal blocks in the inner borderland, which is not inconsistent with geodetic data that suggests a component of extension cross the southern inner borderland, could account for the greater intensity of contractional structures in the hanging wall of the northern OBT west of the SCOZD. This might explain the local reactivation of portions of the OBT, but would not require reactivation or rupture of the entire detachment.

- Much of the contractional deformation observed in the inner borderland (e.g., the San Mateo thrust belt and the Carlsbad thrust) could have occurred during the Pliocene within a different stress regime.

- Regional coastal uplift, which is cited by Rivero and others (2000) to propose that the Oceanside and Thirtymile Bank thrusts are active over a region larger than the San Joaquin Hills, may be attributed to a large degree to other processes (e.g., rift shoulder thermal isostasy). There is no evidence for tilting or significant differential uplift along the coast as recorded by the Quaternary marine terraces and underlying Tertiary bedrock that would indicate movement on an underlying thrust fault.

Global Positioning System Data Evaluation

On the basis of a systematic evaluation of GPS data performed in this study, the following observations can be made with respect to the relative weights assigned to the models in the combined characterization of near-field faulting proximate to the SONGS site:

- The overall patterns of relative displacement rates indicate that no compressional relative displacement fields exist behind the hanging wall side of the OBT postulated as part of Model 2 and Model 3.

- Both the total and incremental relative displacement rates associated with the four selected pairs of SCIGN GPS stations are adequately consistent with the slip rates associated with the postulated Model 1.

- Both the total and incremental relative displacement rates associated with the four selected pairs of SCIGN GPS stations appear to become significantly inconsistent with the slip rates associated with the postulated Model 2 and Model 3, with Model 3 being slightly worse than Model 2. Although for some pairs the consistency may not be too bad for Model 2 and Model 3, it is the overall pattern of consistency that dictates the reasonableness of the postulated seismic sources.

- There may be some compressive straining between some coastal areas near the SONGS site and Catalina Island. However, the reported error ellipses associated with these sites are large enough that the compressive component may well be within the uncertainties, and, in any case, the small compressive straining between the coastal area and Catalina Island is considered inadequate to load or drive the postulated OBT.

- A systematic evaluation of the available GPS data indicates that putting weights to Model 2 and Model 3 higher than those presented in Section 2.0 is not justified. On the contrary, based strictly on the GPS data, one can make a good case for putting weights significantly lower than those presented in Section 2.0 for Model 2 and Model 3.

- Finally, it is noted that where the patterns of GPS relative displacement rates indicate significant unaccounted compressional components in the direction perpendicular to the major strike-slip faults in the region, a conclusion is often reached that thrust faults would likely accommodate the contraction (e.g., Bawden et al., 2001). In the region of the SONGS site, the absence of such patterns of significant GPS relative displacement rates in the direction perpendicular to the major strike-slip faults in the region, as shown in Section 3, is not consistent with the presence of active thrust faults in the area.

Seismic Hazard Analysis Results

Based on the results of the probabilistic seismic hazard analysis reported in Section 4.0 the following observations have been made.

- In general, the hazard curves, response spectra, and weighted hazard curves for the combined OBT case are higher than those from the Model 1 with the differences being greater at lower annual frequency of exceedance levels. Because the combined OBT case results are higher and because the GPS data indicate that the weights used in the combined OBT case are likely too high for models 2 and 3, the results of the 2001 PSHA which use the combined OBT case should be conservative.
- The effects of directivity appear to be no more than about a 8 percent increase in spectral acceleration values at 0.5 Hz and about 2 percent at 1 Hz.
- The effects of fling step appear to be even less at no more than about 2 percent additional increase in spectral values at 0.5 Hz and about a 1 percent additional increase at 1 Hz.

Compared to the SONGS IPEEE response spectrum, the 2001 PSHA response spectrum has higher accelerations at frequencies below 1.5 Hz, but the results are comparable in the frequency range of 1 to 10 Hz as shown on Figure 4-21.

Figure 4-22 shows the 2001 weighted hazard curve for the combined results (Model 1, Model 2, and Model 3) reflecting the directivity and fling step effects. Figure 4-22 also shows the SONGS IPEEE weighted hazard curve for comparison. Overall the 2001 weighted hazard curve is comparable to the SONGS IPEEE weighted hazard curve.

Seismic Probabilistic Risk Analysis

To calculate the risk impact of the postulated blind thrusts, the baseline risk is assessed using the current SONGS Living PRA. This is compared against the postulated risk as assessed by substituting the postulated seismic hazard curve in the current SONGS Living PRA. The risk difference, or risk increase, is evaluated for core damage frequency (CDF) and large, early release frequency (LERF).

From the SONGS 2/3 Living PRA, the current average SONGS CDF and LERF from internal and external events are 4.27E-5/year and 1.60E-6/year, respectively. Substituting the seismic hazard curve to include the postulated blind thrusts results in a total average core damage and large, early release risk of 4.57E-5/year and 1.78E-6/year. These are postulated increases of 3.0E-6/year and 1.8E-7/year.

Although Regulatory Guide 1.174 is only applicable to license change submittals, it provides context to the increase in risk from the postulated seismic hazard curve. Per Regulatory Guide 1.174, an increase of 3.0E-6/year for CDF and 1.8E-7/year for LERF are considered small.

The seismic PRA results show that there would be no vulnerabilities at SONGS and the increase in core damage frequency is small. Therefore, the postulated blind thrusts would not appreciably change the seismic risk of SONGS.

7.0 REFERENCES

Abrahamson, N.A. (1994). Personal communication.

Abrahamson, N.A., and Silva, W.J. (1997). Empirical Response Spectral Attenuation Relations for Shallow Crustal Earthquakes. Seismological Research Letters, Vol. 68, No. 1, Jan./Feb. 1997, pp. 94-127.

Abrahamson, N.A. (2000). Effects of Rupture Directivity on Probabilistic Seismic Hazard Analysis, Proc. Of the 6th International Conf. on Seismic Zonation, Palm Springs, CA, Nov. 2000.

Argus, D. F., and Gordon, R. G., 1988, Sierra Nevada-North America motion from VLBI and paleomagnetic data – implications for the kinematic of the Basin and Range, Colorado Plateau, and California Coast Ranges: EOS Transactions, American Geophysical Union, v 69, p. 1418.

Astiz, L., and Shearer, P. M., 2000, Earthquake location in the Inner Continental Borderland, offshore southern California: Seismological Society of America Bulletin, v. 90, p. 425-449.

Barrie, D., Tatnall, T., and Gath, E., 1992, Neotectonic uplift and ages of Pleistocene marine terraces, San Joaquin Hills, Orange County, California, *in* Heath, P.G., and Lewis, W. L., (eds.), The Regressive Pleistocene Shoreline Coastal Southern California: South Coast Geological Society, Inc., 1992 Annual Field Trip Guide Book No 20, p 115-122.

Bender, E.E., 2000, Late Quaternary uplift and earthquake potential of the San Joaquin Hills, southern Los Angeles basin, California: Comment: Geology, April.

Bohannon, R., and Geist, E., 1998, Upper crustal structure and Neogene tectonic development of the California continental borderland: Geological Society of America Bulletin, v. 110, p. 779-800.

Boore, D.M., Joyner, W.B., and Fumal, T.E. (1994). Estimation of Response Spectra and Peak Accelerations from Western North American Earthquakes: An Interim Report, Part 2. U.S. Geological Survey, *Open-File Report 94-127.*

Boore, D.M., Joyner, W.B., Fumal, T.E. (1997). Equations for Estimating Horizontal Response Spectra and Peak Acceleration from Western North American Earthquakes: A Summary of Recent Work. Seismological Research Letters, Vol. 68, No. 1, Jan./Feb. 1997, pp. 128-153.

Bozorgnia, Y., Campbell, K.W., and Niazi, M. (1999). Vertical Ground Motion: Characteristics, Relationship with Horizontal Component, and Building-Code Implications. Proc. of the SMIP99 Seminar on Utilization of Strong-Motion Data, Sept.

15, 1999, Oakland, CA, California Strong Motion Instrumentation Program, Sacramento, CA, pp. 23-29.

Campbell, K.W. (1993). Empirical Prediction of Near Source Ground Motion from Large Earthquakes, *International Workshop on Earthquake Hazard ad Large Dams in the Himalaya*, January 15-16, 1993, New Delhi, India, Indian National Trust for Art and Cultural Heritage (INTACH).

Campbell, K.W., and Bozorgnia, Y. (1994). Near-Source Attenuation of Peak Horizontal Acceleration from Worldwide Accelerograms, *Fifth U.S. National Conference on Earthquake Engineering*, Chicago, Illinois, July 10-14, 1994.

Clarke, S. H., Greene, H. G., Kennedy, M. P., and Vedder, J. G., (with contributions by Legg, M. R.), 1987, Geologic map on the inner-southern California continental margin, California Continental Margin Geologic Map Series: California Division of Mines and Geology, Maps 1A, 1B, 1C, 1D.

Cornell, C.A. (1968). Engineering seismic risk analysis, *Bull. of the Seismological Soc. of America*, Vol. 58, No. 5, pp. 1583-1606.

Coppersmith, K.J., and Youngs, R.R. (1986). Capturing uncertainty in probabilistic seismic hazard assessments within intraplate tectonic environments, *Proc. of the Third U.S. National Conf. on Earthquake Eng.*, Charleston, SC, Vol. 1, pp. 301-302.

Crouch, J. K., and Bachman, S. B., 1989, Exploration potential offshore Newport-Inglewood fault zone (abs.): American Association of Petroleum Geologists Bulletin, v. 73, p. 536.

Crouch, J. K., and Suppe, J., 1993, Late Cenozoic tectonic evolution of the Los Angeles basin and Inner California Borderland: A model for core complex-like crustal extension: Geological Society of America Bulletin, v. 105, p. 1415-1434.

DeMets, C. R., Gordon, G., Argus, D F, and Stein, S, 1990, Current plate motions: Geophysical Journal International, v 101, p. 425-478.

Ehlig, P. L., and Farley, T.,1978, Geology map adjacent to San Onofre Nuclear Generating Station, unpublished.

Ehlig, P. L.,1977, Geologic report on the area adjacent to the San Onofre nuclear generating station, northwestern San Diego, California: Los Angeles, Southern California Edison Company, 40 p.

Fischer, P. J., and Lee, C. 1992, Evolution of Santa Monica-San Pedro Margin, California during the last 25,000 yr, *in* Heath, E. G., and Lewis, W. I., (eds.), The Regressive Pleistocene Shoreline Coastal Southern California: South Coast Geological Society, Inc., 1992 Annual Field Trip Guide Book No. 20, p. 161-194.

Fischer, P.J., and Mills, G.I., 1991, The offshore Newport-Inglewood-Rose Canyon fault zone, California: Structure, segmentation and tectonics, *in* Abbott, P.L., and Elliott, W.J. (eds.), Environmental Perils, The San Diego Region: San Diego Association of Geologist, San Diego, California, p. 17-36.

Grant, L., Mueller, K., Munro, R., Gath, E., Kennedy, G., and Edwards, L., 1997, Geomorphic and structural analysis of the San Joaquin Hills in Orange County, California: SCEC Annual Meeting Field Trip Guidebook, October 5, 1997.

Grant, L. B., Mueller, K. J., Gath, E. M., Cheng, H., Edwards, R. L., Munro, R., and Kennedy, G., 1999, Late Quaternary uplift and earthquake potential of the San Joaquin Hills, southern Los Angeles basin, California: Geology, v. 27, p. 1031-1034.

Grant, L. B., Mueller, K. L., Gath, E. M., and Munro, R., 2000, Late Quaternary uplift and earthquake potential of the San Joaquin Hills, southern Los Angeles basin, California: Reply: Geology, April.

Grant, L. B., Ballenger, L J., and Runnerstrom, E E., in press, Coastal uplift of the San Joaquin Hills, southern Los Angeles Basin, California, by a large earthquake since 1635 A. D.: submitted to the Bulletin of the Seismological Society of America.

Greene, H. G., Bailey, K. A., Clarke, S. H., Ziony, J. I., and Kennedy, M.P., 1979, Implications of fault patterns of the inner California continental borderland between San Pedro and San Diego, *in* Abbott, P. L. and Elliot, W. J., (eds.), Earthquakes and other Perils, San Diego Region: Geological Society of America field trip guidebook published by San Diego Association of Geologists, p. 21-28.

Hauksson, E., and Gross, S., 1991, Source parameters of the 1933 Long Beach earthquake: Bulletin of the Seismological Society of America, v. 81, p. 81-98.

Hudnut, K.W., Shen, Z., Murray, M., McClusky, S., King, R., Herring, T., Hager, B., Feng, Y., Fang, P., Donellan, A., and Bock, Y. (1996). Co-Seismic Displacements of the 1994 Northridge, California, Earthquake, Bull. of the Seism. Soc. of America, Vol. 86, No. 1B, pp. S19-S36, Feb. 1996.

Idriss, I.M. (1985). "Evaluating Seismic Risk in Engineering Practice", *Proc. Eleventh International Conf. on Soil Mech. and Found. Eng.*, August 12-16, 1985, San Francisco, California, 1, pp. 255-320, A.A. Balkema, Rotterdam.

Idriss, I.M. (1987). Earthquake Ground Motions, Lecture notes, Course on Strong Motion, Earthquake Engineering Research Institute, Pasadena, California, April 10-17, 1987.

Idriss, I.M. (1994). Personal communication.

Jennings, C. W., 1992, Preliminary fault activity map of California: California Division of Mines and Geology Open-File Report 92-03, scale 1:750,000.

Kennedy, G. L.,1975, Geology of the San Diego Metropolitan Area, California: California Division of Mines and Geology, Bulletin 200, Part A, 56 p.

Kennedy and others, 1975, Character and recency of faulting, San Diego metropolitan area, California: California Division of Mines and Geology Special Report 123, 33 p.

Kern, J. P., and Rockwell, T. K., 1992, Chronology and deformation of Quaternary marine shorelines, San Diego county, California, *in* Heath, E., and Lewis, L., (eds.), The regressive Pleistocene shoreline in southern California: Santa Ana, California, South Coast Geological Society Annual Field Trip Guidebook 20, p. 1-7.

Kier, G., and Mueller, K., 1999, Evidence for active shortening in the offshore Borderlands and its implications for blind thrust hazards in the Coastal Orange and San Diego Counties, 1999 Southern California Earthquake Center-SCEC Annual Meeting: Los Angeles, Southern California Earthquake Center, Proceedings and Abstracts, p. 71.

Kier, G., Mueller, K., and Rockwell, T., Origin of regional uplift across Southern California and Northern Baja California: submitted to Tectonics, 2001, in review.

Kulkarni, R.B., Sadigh, K., and Idriss, I.M. (1979). Probabilistic evaluation of seismic exposure, *Proc. of the Second U.S. National Conf. on Earthquake Eng.*, Stanford, CA, August 22-24, pp. 90-99.

Kulkarni, R.B., Youngs, R.R., Coppersmith, K.J. (1984.) Assessment of Confidence Intervals for Results of Seismic Hazard Analysis, *Proc. 8th World Conf. on Earthquake Eng.*, Vol. I, pp. 263-270.

Lajoie, K. R., Kern, J.P., and Wehmiller, J. F., 1979, Quaternary marine shorelines and crustal deformation, San Diego to Santa Barbara, California, *in* Abbott, P., ed., Geologic excursions in the southern California area: San Diego, California, San Diego State University, p. 3-15.

Lajoie, K. R., Ponti, D. J., Powell, C.L., Mathieson, S. A., and Sarna-Wojcicki, A..M., 1992, Emergent marine strandlines and associated sediments, coastal California: A record of Quaternary sea-level fluctuations, vertical tectonic movements, climatic changes and coastal processes, *in* Heath, E., and Lewis, L., (eds.), The regressive Pleistocene shoreline in southern California: Santa Ana, California, South Coast Geological Society annual Field Trip guidebook 20, p. 81-104.

Legg, M., 1991, Developments in understanding the tectonic evolution of the California continental borderland: SEPM Special Publication No. 46, p. 291-312.

Legg, M., and Kennedy, M.P., 1991, Oblique divergence and convergence in the California continental borderland, *in* Abbott, P. L., and Elliott, W. J., (eds.), Environmental Perris San Diego Region: San Diego Association of Geologists, San Diego, California, p. 1-16.

Legg, M., Nicholson, C., and Sorlien, C., 1992, Active faulting and tectonics of the Inner California Continental Borderland: USGS lines 114 and 112: Eos (Transactions, American Geophysical Union), v. 73, p. 588.

Lettis, W. R, and Hanson, K. L., 1991, Crustal strain partitioning: implications for seismic-hazard assessment in western California: Geology, v. 19, p. 559-562.

Lindvall, S. C., Rockwell, T. K., and Lindvall, C. E., 1990, The seismic hazard of San Diego revised: new evidence for magnitude 6+ Holocene earthquakes on the Rose Canyon fault zone: Proceedings, 4 th U.S. Conference on Earthquake Engineering.

Medwedeff, D., 1992, Geometry and kinematics of an active, laterally propagating wedge thrust, Wheeler Ridge, California, *in* Mitra, S., and Fischer, G. W., (eds.), Structural geology of fold and thrust belts: Baltimore, Maryland, Johns Hopkins University Press, p 3-28.

Mesa 2 Inc., 1985 (revised), Southern California Inner Margin Project (SCIMAP), Maps 10-13.

Moore, G.W., 1972, Offshore extension of the Rose Canyon fault, San Diego, California: United States Geological Survey Professional Paper 800-C, p. C113-116.

Moore, D., 1980, Edited transcript of Dr. D. Moore discussion of offshore recent seismic reflection profiles, September 23, 1980: Appendix I, San Onofre 2&3 Updated FSAR, Rev. 16, p. 2:5I-27-50.

Morton, P.K., and Miller, R. V., 1981, Geologic map of Orange County, California, showing mines and mineral deposits: California Department of Conservation, Division of Mines and Geology, Bulletin 204, Plate 1 (scale 1:48,000).

Mueller, K., 1997, Recency of folding along the Compton-Los Alamitos Trend: implications for seismic risk in the Los Angeles Basin (abs.): EOS, Transactions of the American Geophysical Union, v. 78, p. 702.

Mueller, K.J., Grant, L.B., and Gath, E., 1998a, Late Quaternary Growth of the San Joaquin Hills Anticline—A new source of blind thrust earthquakes in the Los Angeles basin: Seismological Research Letters, v. 69, no. 2, p. 161.

Mueller, K., Shaw, J., and Rivera, C., 1998b, Determining the geometry of the San Joaquin Hills blind thrust: implications for earthquake source characteristics: unpublished progress report submitted to Southern California Earthquake Center, February 23, 1998.

Nicholson, C., Sorlien, C. and Legg, M., 1993, Crustal imaging and extreme Miocene extension of the Inner California Continental Borderland: Geological Society of America Abstracts with Programs, v. 25, no. 6, p. A-418.

Nicholson, C., Sorlien, C., Atwater, T., Crowell, J., and Luyendyk, B.P, 1994, Microplate capture, rotation of the western Transverse Ranges, and initiation of the San Andreas transform as a low-angle fault system: Geology, v. 22, p. 491-495.

Nicholson, C., Sorlien, C., Kamerling, M.J., and Legg, M.R., 1996, Crustal imaging along the Southern California margin: Miocene extension, rotation, and tectonic inversion related to an evolving transform system: EOS Transactions of the American Geophysical Union, v. 77, no. 46, p. F738.

NRC (S. Dembeck) to SCE (H. B. Ray) letter dated August 2, 2001, Subject: San Onofre Nuclear Generating Station Seismic Design Basis.

Pacific Gas and Electric Company (PG&E), 1990, Response to Questions on the Final Report of the Diablo Canyon Long Term Seismic Program: U.S. Nuclear Regulatory Commission Docket Nos. 50-275 and 50-323.

Ponti, D. J., 2001, Changing deformation rates through time: Insights from new Quaternary stratigraphic studies in the Los Angeles Basin, California, (abs.): EOS Transactions of the American Geophysical Union, v. 82, no. 47, Fall Meeting Supplement, Abstract S12E-11.

Reiter, L. (1990). Earthquake Hazard Analysis, Issues and Insights. Columbia University Press, New York, 254 p.

Risk Engineering, Inc., 1995, Seismic hazard at San Onofre Nuclear Generating Station: Prepared for Southern California Edison Company, August 25.

Rivero, C., Shaw, J. H., and Mueller, K., 2000, Oceanside and Thirtymile Bank blind thrusts: Implications for earthquake hazards in coastal southern California: Geology, v. 28, p. 891-894.

Rivero, C. and Shaw, J. H., 2001, 3D geometry and seismogenic potential of the Inner California Borderland blind thrusts system : 2001 SCEC Annual Meeting Proceedings and Abstracts, p. 105-106.

Rockwell, T.K., Lindvall, S.C., Haraden, C.C., Hirabayashi, C.K., and Baker, E., 1991, Minimum Holocene slip rate for the Rose Canyon fault in San Diego, California, *in* Abbott, P.L., and Elliott, W.J. (eds.), Environmental Perils, The San Diego Region: San Diego Association of Geologists, San Diego, California, p. 37-46.

Rockwell, T.K., Lindvall, S. C., Haraden, C.C., Hirabyashi, C. K., and Baker, E., 1992,

Minimum Holocene slip rate for the Rose Canyon fault in San Diego, California, *in* Heath, E. G., and Lewis, W. L., (eds.), The Regressive Pleistocene Shoreline Coastal Southern California: South Coast Geological Society, Inc., 1992 Annual field Trip Guide Book No. 20, p. 55-64.

Sadigh, K. (1994). Personal communication.

Sadigh, K., Chang, C.-Y., Egan, J.A., Makdisi, F., and Youngs, R.R. (1997). Attenuation Relationships for Shallow Crustal Earthquakes Based on California Strong Motion Data. Seismological Research Letters, Vol. 68, No. 1, Jan./Feb. 1997, pp. 180-189.

Shaw, J., and Suppe, J., 1996, Earthquake hazards of active blind-thrust faults under the central Los Angeles basin, California: Journal of Geophysical Research, v. 101, no. B4, p. 8623-8642.

Shlemon, R.J., 1992, The Cristianitos fault and Quaternary geology, San Onofre State Beach, California, *in* Heath, E.G., and Lewis, W.L., (eds.), The Regressive Pleistocene Shoreline, Southern California: South Coast Geological Society, Inc. Annual Field Trip Guide Book No. 20, p. 9-12.

Sliter, R. W., Ryan, H. F., and Normark, W. R., 2001, Does recent deformation at the base of slope provide evidence of a connection between the Newport-Inglewood and the Rose Canyon fault zones offshore southern California?: Eos Trans. AGU, v. 82, no 47, Fall Meet. Suppl., Abstract S11A-0531, 2001.

Somerville, P.A., Smith, N.A., Graves, R.W., and Abrahamson, N.A. (1997). Modification of Empirical Strong Ground Motion Attenuation Relationships to include the Amplitude and Duration Effects of Rupture Directivity. Seismological Research Letters, Vol. 68, No. 1, January/February, pp. 199-222.

San Onofre Nuclear Generating Station, Units 2 and 3 (SONGS 2&3), Updated Final Safety Analysis Report (FSAR), Rev. 16; Section 2.5, Geology, Seismology and Geotechnical Engineering.

SCE (W. C. Marsh) to NRC letter dated December 15, 1995, Subject: Response to Generic Letter 88-20, Supplement 4, Individual Plant Examination of External Events (IPEEE), San Onofre Nuclear Generating Station, Units 2 and 3.

SCE (D. E. Nunn) to NRC letter dated September 21, 2001, Subject: Seismic Design Basis Assessment, San Onofre Nuclear Generating Station, Units 2 and 3.

Stein, R. and Ekstrom, G., 1992, Seismicity and geometry of a 110 km-long blind thrust fault, 2, Synthesis of the 1982-1985 California earthquake sequence, Journal of Geophysical Research, v. 97, p. 4865-4883.

Stein, R. S., and Yeats, R. S, 1989, Hidden earthquakes: Scientific American, v 260, no. 6, p. 48-57.

Stuart, C. J., 1979a, Middle Miocene paleogeography of coastal southern California and the California borderland – Evidence from schist-bearing sedimentary rocks, *in* Armentrout, J. M., Cole, M. R., and TerBest, H., Jr., (eds.), Cenozoic paleogeography of the western United States: Society of Economic Paleontologists and Mineralogists, Pacific Section, Pacific Coast Paleogeography Symposium 3, p. 29-44.

Stuart, C. J., 1979b, Lithofacies and origin of the San Onofre Breccia, coastal southern California, *in* Stuart, C. J., (ed.), A guidebook to Miocene lithofacies and depositional environments, coastal southern California and northwestern Baja California: Society of Economic Paleontologists and Mineralogists, Pacific Section, p. 25-42.

Vedder, J.G., Yerkes, R. F., and Schoelhamer, J. E., 1957, Geologic map of San Joaquin-San Juan Capistrano area, Orange County, California: U. S. Geological Survey Oil and Gas Investigations Map, OM 193, scale 1:24,000.

Vedder, J. G., 1975, Revised geologic map, structure sections, and well table, San Joaquin Hills-San Juan Capistrano area, California: U. S. Geological Survey Open-File Report 75-552, 5 sheets, scale 1:24,000.

Vedder, J. G., and Howell, D.G., 1976, Review of the distribution and tectonic implications of Miocene debris from the Catalina Schist, California Continental Borderland and adjacent coastal areas, *in* Howell, D. G.,(ed.), Aspects of the geologic history of the California Continental Borderland: American Association of Petroleum Geologists, Pacific Section, Miscellaneous Publication 24, p. 326-342.

Weldon, R., and Humphreys, E., 1986, A kinematic model of southern California: Tectonics, v. 5, p. 33-48.

Wells, D. L., and Coppersmith, K. J., 1991, Analysis of fault dip and sense of slip for historical earthquakes, (abs.): Seismological Research Letters, v. 62, p. 38.

Wells, D. L., and Coppersmith, K. J., 1994, New empirical relationships among magnitude, rupture length, rupture width, rupture area, and surface displacement: Bulletin of the Seismological Society of America, v. 84, no. 4, p. 974-1002.

West, J. C., 1979, Supplement to the generalized sub-surface geological and geophysical study Capistrano Area Orange County, California, January 1979: Appendix 2.5H of San Onofre, Units 2 and 3, Updated FSAR, Rev 16.

Western Geophysical Company, 1972, Final Report: San Onofre offshore investigations, submitted to Southern California Edison and San Diego Gas & Electric Company, March 1, 1972.

Woodward-Clyde Consultants, 1979, Report of the evaluation of maximum earthquake and site ground motion parameters associated with the offshore zone of deformation, San Onofre Nuclear Generating Station, unpublished report prepared for Southern California Edison.

Ziony, J. I., Wentworth, C. M., Buchanan-Banks, J. M., and Wagner, H. C., 1974, Preliminary map showing recency of faulting in coastal southern California: United States Geological survey Miscellaneous Field Studies Map MF-585.

Zoback, M. L., Anderson, R. E., and Thompson, G. A., 1981, Cenozoic evolution of the state of stress and style of tectonism in the western United States: Philosophical Transactions of the Royal Society of London, Ser. A., v. 300, p. 407-434.